Computer Modeling in Engineering & Sciences

Tech Science Press

DOI: 10.32604/cmes.2023.029044

ARTICLE

Parameters Optimization and Performance Evaluation of the Tuned Inerter Damper for the Seismic Protection of Adjacent Building Structures

Xiaofang Kang[1,*], Jian Wu[1], Xinqi Wang[1] and Shancheng Lei[2]

[1]Key Laboratory of Intelligent Underground Detection Technology, School of Civil Engineering, Anhui Jianzhu University, Hefei, 230601, China

[2]Chengnan College, Changsha University of Science and Technology, Changsha, 410015, China

*Corresponding Author: Xiaofang Kang. Email: xiaofangkang@ahjzu.edu.cn

Received: 28 January 2023 Accepted: 22 May 2023 Published: 22 September 2023

ABSTRACT

In order to improve the seismic performance of adjacent buildings, two types of tuned inerter damper (TID) damping systems for adjacent buildings are proposed, which are composed of springs, inerter devices and dampers in serial or in parallel. The dynamic equations of TID adjacent building damping systems were derived, and the H_2 norm criterion was used to optimize and adjust them, so that the system had the optimum damping performance under white noise random excitation. Taking TID frequency ratio and damping ratio as optimization parameters, the optimum analytical solutions of the displacement frequency response of the undamped structure under white noise excitation were obtained. The results showed that compared with the classic TMD, TID could obtain a better damping effect in the adjacent buildings. Comparing the TIDs composed of serial or parallel, it was found that the parallel TIDs had more significant advantages in controlling the peak displacement frequency response, while the H_2 norm of the displacement frequency response of the damping system under the coupling of serial TID was smaller. Taking the adjacent building composed of two ten-story frame structures as an example, the displacement and energy collection time history analysis of the adjacent building coupled with the optimum design parameter TIDs were carried out. It was found that TID had a better damping effect in the full-time range compared with the classic TMD. This paper also studied the potential power of TID in adjacent buildings, which can be converted into available power resources during earthquakes.

KEYWORDS

Adjacent buildings; tuned inerter damper (TID); H_2 norm optimization; vibration control; energy harvesting

1 Introduction

Since Lee et al. first proposed the method of vibration control for civil structures in 1972 [1], the theory and method of vibration control have been developed rapidly. In order to deal with structural vibration problems caused by wind load or earthquake load, a series of control strategies have been formed, including active control, passive control, hybrid control, and intelligent control [2]. Among them, passive vibration control is widely used in engineering practice because of its high stability, low cost, good control effect, and easy realization [3,4]. The design of classic tuned mass damper (TMD)

consists of a mass block, spring and viscous damper, which is a reliable structural vibration control device [5]. Kareem et al. took high-rise buildings subjected to wind load as an example, introduced the application of TMDs in Australia, Canada, China, Japan, and the United States in recent years, and showed that TMD had superior seismic performance [6]. However, for TMD, to obtain better and more robust control performance, it is necessary to use a larger auxiliary mass, that is, to increase the mass ratio of TMD to the controlled structure, which is often restricted by site conditions or costs [7]. In order to solve the problems encountered in the practical application of TMD, researchers have developed many new dampers based on the existing TMD research, including electromagnetic inertial mass damper (EIMD) [8,9], rotational inertial damper (RID) [10,11], rotational inertial double-tuned mass damper (RIDTMD) [12–14], tuned mass damper inerter (TMDI) [15–17], tuned liquid inerter system (TLIS) [18], tuned inerter damper (TID) [19–23], tuned mass-inerter damper (TMID) [24], tuned fluid inerter (TFI) [25,26], clutching inerter damper (CID) [27], etc. These dampers introduced a promising passive vibration control device, namely inerter device.

Inerter device is a mechanical device with two ends which was first proposed by Smith in 2002 [28]. Its characteristic is that the applied inerter force is proportional to the relative acceleration between the two ends, and it usually consists of rack and pinion, ball screw and hydraulic mechanism [12,29,30]. Inerter devices have significant mass amplification effect, and the effective mass produced can exceed 100 times of its physical mass [13,31,32]. The principle of the inerter device is that it can transform the linear motion of both ends of the device into the rotational motion of the flywheel when an earthquake occurs, resulting in considerable inerter [33–35]. For example, Ikago et al. realized an apparent mass of 300 kg with a ball screw device with a physical mass of only 2 kg [36], Javidialesaadi et al. designed and produced a ball screw mechanism with a physical mass of only 2 kg to produce an effective mass of 350 kg [13]. It can be seen that in order to produce an equivalent effective mass, the actual physical mass of the inerter device is far less than that of the traditional TMD. In addition, the research also showed that when the TID is placed at the bottom of the main structure, the performance of the TID is the best, which is opposite to the TMD that must be placed at the position where the maximum displacement occurs, that is, the top of the structure [22]. TID can obtain a large inerter mass ratio without increasing the physical mass, so it is considered that TID can replace the traditional TMD and be applied in engineering practice. Based on inerter device, Dai et al. explored the optimal design of Maxwell tuned-mass-damper-inerter (M-TMDI) to mitigate vortex-induced vibration (VIV) of bridges. Based on a two-DOF system, the optimal parameters of a specific M-TMDI, in which the end of the inerter is connected to the fixed ground, are analytically given using the inerter location as a design variable [37]. In addition, Dai et al. aimed at the impact of the location of inerter on the control performance of tuned mass-damping-inerter (TMDI) in wind-induced vibration mitigation of flexible structures, discussed the control effect, optimum design parameters, and high-mode damping effects of the TMDI [38]. Different types of control devices based on inerter devices are also used in base isolated structures. TIDs are installed at the bottom of the structure to further reduce the displacement of isolated floors and the inter story displacement of superstructure [35,39,40]. Among them, the inerter device based on the generator device can collect energy while reducing the displacement of the upper structure, realizing the trade-off between the two contradictory goals of energy collection and vibration control [35]. Gonzalez-Buelga et al. proposed a circuit containing both damping and energy collection effects, and connected it with the electromagnetic transducer to synthesize TID, which also achieved the dual goals of damping and energy collection [41]. Unlike TMD driven by the absolute motion of the damper, TID is driven by the relative motion between the two ends of the device, which actually provides conditions for the corresponding energy collection mode of TID [42].

In order to achieve the best control effect of the vibration control device, different types of optimization methods have been proposed, including the most commonly used method, namely H_2 norm optimization. The H_2 optimization criterion was first proposed by Crandall and Mark in 1963 and applied to the design of dynamic vibration absorbers (DVAs), with the goal of reducing the total vibration energy of the system at all frequencies [43]. It can be understood that if the vibration control system is subjected to random excitation, that is, the excitation contains an infinite number of frequencies, then it is unnecessary to consider only the resonance frequency of the system. Under this optimization criterion, the area under the frequency response curve of the system (called H_2 norm) is the smallest [44]. In the study of vibration control of adjacent buildings based on inerter, Palacios-Quiñonero et al. proposed a computational strategy to design inerter-based multi-actuation systems for the seismic protection of adjacent structures based on an H∞ cost-function and used a constrained global-optimization solver to compute parameter configurations with high-performance characteristics. The research results fully demonstrate the flexibility and effectiveness of the proposed design methodology, and clearly show the superior performance and robustness of the TID actuation systems [45]. Djerouni et al. proposed a new configuration of TMDIs with the goal of studying the seismic response of two adjacent buildings and the pounding distance between them. The results show that the proposed method is effective and better than the existing TID configuration, filling a gap in the research of investigating the effectiveness of TMDI in controlling seismic pounding and the impact of ground motion variability [46]. Taking adjacent buildings as controlled structures, this paper investigated the vibration control performance of serial TID and parallel TID in adjacent buildings. Also, the analytical solutions of the optimum frequency ratio and damping ratio of structural vibration control under random excitation were obtained by using the H_2 norm optimization method. In addition, for the convenience of analysis, the random excitation used in this paper is white noise excitation when analyzing the frequency response of the system.

The main contents of this paper are summarized as follows: First, the analytical solutions of the optimum frequency ratio and the optimum damping ratio of adjacent building structures under the coupling of serial TID and parallel TID were obtained by using the H_2 optimization method. Secondly, the influence of different structural parameters on the optimum solutions was studied. Then, the classic TMD was introduced to compare with the two types of TID, and the frequency response of adjacent building structures under different damper coupling was analyzed. At the same time, the influence of damper mass was also considered. Then, by changing the optimum frequency ratio and the optimum damping ratio, the robust performance of vibration of adjacent buildings under TID coupling was analyzed. Finally, four types of seismic waves were used to analyze the time history of vibration control of adjacent building structures under two types of TIDs and classic TMD coupling, and the time history of energy collection of adjacent building structures under two types of TIDs coupling was analyzed.

2 Mathematical Model

2.1 Simplified Model of Adjacent Buildings

As shown in Fig. 1a is the simplified model of adjacent buildings, where $m_{Li}(i = 1, 2, \ldots, n)$, $c_{Li}(i = 1, 2, \ldots, n)$ and $k_{Li}(i = 1, 2, \ldots, n)$ are the corresponding mass, damping and stiffness of the i floor of the left building respectively; $m_{Ri}(i = 1, 2, \ldots, n)$, $c_{Ri}(i = 1, 2, \ldots, n)$ and $k_{Ri}(i = 1, 2, \ldots, n)$ are the corresponding mass, damping and stiffness of the i floor of the right building respectively; $c_{sj}(j = 1, 2, \ldots, n)$ and $k_{sj}(j = 1, 2, \ldots, n)$ are the corresponding damping and stiffness of the j floor of adjacent buildings. Under the excitation of seismic acceleration $\ddot{x}_g$, in order to better analyze the vibration control effect of dampers on adjacent building structures, the left and right buildings are

simplified into single degree of freedom structures, with their mass, stiffness, and damping values corresponding to the main modes of the structure [47,48]. The simplified model is shown in Fig. 1b. After simplification, the mass, damping and stiffness of the left building are m_1, c_1 and k_1, respectively, and the mass, damping and stiffness of the right building are m_2, c_2 and k_2, respectively. The damping and stiffness between the two buildings are c_s and k_s, respectively.

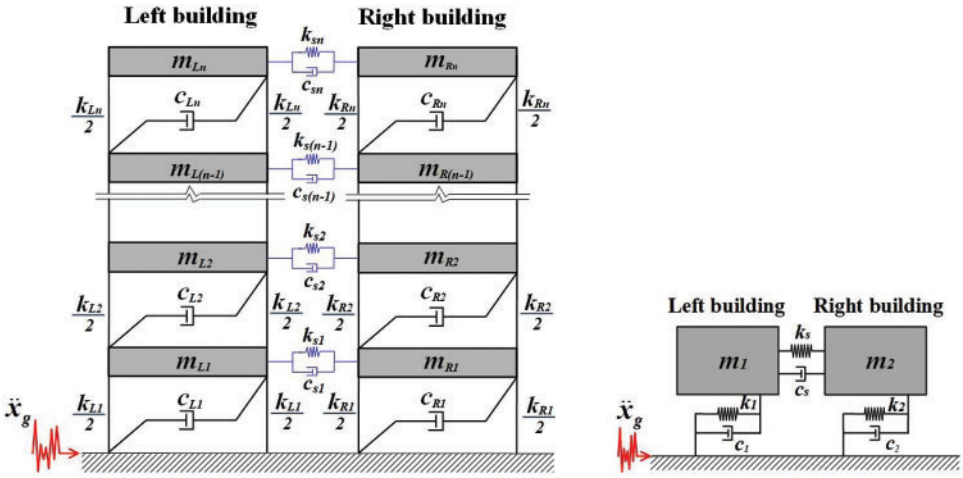

(a) (b)

Figure 1: Simplified schematic graph of adjacent building structures

2.2 Inerter Device Concept

Adding ball screw mechanism (including shell and linear guide rail), flywheel and rotary generator inside the damper can transform the relative linear motion between the structure and the ground into rotation when an earthquake occurs, and drive the flywheel and generator to collect energy [35]. The rotating generator and flywheel drive the inerter mass to rotate, and generate resistance to the driving structure. The damper is elastically installed with the structure, which is equivalent to a spring. Fig. 2a shows a simplified model of the inerter device. It is characterized in that the generated force is proportional to the difference of acceleration at both ends [22]. The mechanical equation can be expressed as:

$$F = b\left(\ddot{x}_l - \ddot{x}_r\right) \tag{1}$$

where x_l, x_r are the displacement of the left and right ends of the inerter device, the symbol ".." denotes the calculation of the second derivative, and b denotes the effective mass.

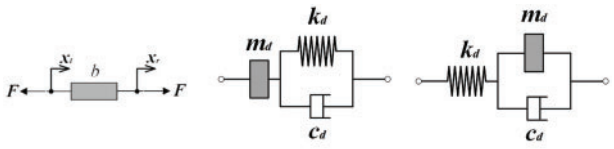

(a) (b) (c)

Figure 2: Inerter device and two types of inerter-based damper models: (a) Inerter device; (b) Serial TID; (c) Parallel TID

2.3 Damping System

According to Section 2.2, considering different connection modes, two damper models with different configurations based on inerter are formed. According to the different positions of m_d and k_d, serial connection of m_d and c_d is called serial TID, and parallel connection of m_d and c_d is called parallel TID. The two TID models are shown in Figs. 2b and 2c, where m_d is the effective mass of TID, c_d and k_d is the damping and stiffness of TID, respectively. Couple the different types of TIDs mentioned above with the simplified adjacent buildings, and the formed models are shown in Fig. 3, where x_1, x_2 and x_d are the displacement of left building, right building and TID under earthquake excitation, respectively.

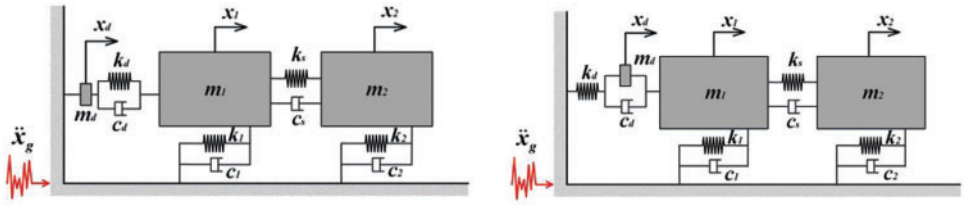

Figure 3: The damping system of adjacent buildings coupled with TID: (a) Serial TID damping system; (b) Parallel TID damping system

3 Parameter Optimization Based on H_2 Norm Criterion

3.1 Equation Establishment

According to the coupled damping system in Fig. 3, the dynamic balance equation of the system can be listed. We stipulate that the structure on the left which connected to TID is the left structure, and the structure on the right of adjacent buildings is the right structure, and they will be distinguished by left structure and right structure in subsequent expressions.

3.1.1 Serial TID

According to the balance principle of force, the dynamic balance equation can be obtained as follows:

$$\begin{cases} m_1\ddot{x}_1 + m_d\ddot{x}_d + c_1\dot{x}_1 + c_s(\dot{x}_1 - \dot{x}_2) + k_1x_1 + k_s(x_1 - x_2) = -m_1\ddot{x}_g \\ m_2\ddot{x}_2 + c_2\dot{x}_2 + c_s(\dot{x}_2 - \dot{x}_1) + k_2x_2 + k_s(x_2 - x_1) = -m_2\ddot{x}_g \\ m_d\ddot{x}_d + c_d(\dot{x}_d - \dot{x}_1) + k_d(x_d - x_1) = 0 \end{cases} \tag{2}$$

After dimensionless transformation by Laplace transform, the following results are obtained:

$$\begin{cases} X_1(i\omega)^2 + \dfrac{m_d}{m_1}X_d(i\omega)^2 + \dfrac{c_1}{m_1}X_1(i\omega) + \dfrac{c_s}{m_1}(X_1 - X_2)(i\omega) + \dfrac{k_1}{m_1}X_1 + \dfrac{k_s}{m_1}(X_1 - X_2) = -\ddot{X}_g \\ \dfrac{m_2}{m_1}X_2(i\omega)^2 + \dfrac{c_2}{m_1}X_2(i\omega) + \dfrac{c_s}{m_1}(X_2 - X_1)(i\omega) + \dfrac{k_2}{m_1}X_2 + \dfrac{k_s}{m_1}(X_2 - X_1) = -\dfrac{m_2}{m_1}\ddot{X}_g \\ \dfrac{m_d}{m_1}X_d(i\omega)^2 + \dfrac{c_d}{m_1}(X_d - X_1)(i\omega) + \dfrac{k_d}{m_1}(X_d - X_1) = 0 \end{cases} \tag{3}$$

Define some new parameters for the next transformation. The defined parameters are shown in Table 1. After substituting them into Eq. (3), there are:

$$\begin{cases} X_1 (i\alpha)^2 + \beta_d X_d (i\alpha)^2 + 2\xi_1 X_1 (i\alpha) + 2\mu_s \xi_1 (X_1 - X_2)(i\alpha) + X_1 + \lambda_s (X_1 - X_2) = -\dfrac{\ddot{X}_g}{\omega_1^2} \\ \beta_2 X_2 (i\alpha)^2 + 2\mu_2 \xi_1 X_2 (i\alpha) + 2\mu_s \xi_1 (X_2 - X_1)(i\alpha) + \lambda_2 X_2 + \lambda_s (X_2 - X_1) = -\dfrac{\beta_2 \ddot{X}_g}{\omega_1^2} \\ \beta_d X_d (i\alpha)^2 + 2\beta_d \xi_d f_d (X_d - X_1)(i\alpha) + \lambda_d (X_d - X_1) = 0 \end{cases} \tag{4}$$

Table 1: Parameters and their definitions during derivation

Parameters	Definition	Description
β_2	$\beta_2 = m_2/m_1$	Ratio of right structure mass to left structure mass
β_d	$\beta_d = m_d/m_1$	Ratio of inerter mass to left structure mass
u_2	$u_2 = c_2/c_1$	Ratio of right structure damping to left structure damping
u_s	$u_s = c_s/c_1$	Ratio of TID damping to left structure damping
ξ_1	$\xi_1 = c_1/2\sqrt{k_1 m_1}$	Damping ratio of left structure
ξ_d	$\xi_d = c_d/2\sqrt{k_d m_d}$	Nominal damping ratio of TID
λ_2	$\lambda_2 = k_2/k_1$	Ratio of right structure stiffness to left structure stiffness
λ_s	$\lambda_s = k_s/k_1$	Ratio of stiffness between adjacent buildings to stiffness of left structure
λ_d	$\lambda_d = k_d/k_1$	Ratio of stiffness of TID to stiffness of left structure
ω_1	$\omega_1 = \sqrt{k_1/m_1}$	Natural frequency of left structure
ω_d	$\omega_d = \sqrt{k_d/m_d}$	Nominal frequency of TID
ω	—	External excitation frequency
f_d	$f_d = \omega_d/\omega_1$	Ratio of TID nominal frequency to left structure frequency
α	$\alpha = \omega/\omega_1$	Normalized frequency
i	—	Imaginary unit
X_1, X_2, X_d	—	The form of x_1, x_2 and x_d after Laplace transformation

3.1.2 Parallel TID

According to the balance principle of force, the dynamic balance equation can be obtained as follows:

$$\begin{cases} m_1 \ddot{x}_1 + c_1 \dot{x}_1 + c_s (\dot{x}_1 - \dot{x}_2) + k_1 x_1 + k_s (x_1 - x_2) + k_d x_d = -m_1 \ddot{x}_g \\ m_2 \ddot{x}_2 + c_2 \dot{x}_2 + c_s (\dot{x}_2 - \dot{x}_1) + k_2 x_2 + k_s (x_2 - x_1) = -m_2 \ddot{x}_g \\ m_d (\ddot{x}_1 - \ddot{x}_d) + c_d (\dot{x}_1 - \dot{x}_d) - k_d x_d = -m_d \ddot{x}_g \end{cases} \tag{5}$$

Similar to the serial TID, it can be obtained from Table 1 and Eq. (5) as follows:

$$\begin{cases} X_1(i\alpha)^2 + 2\xi_1 X_1(i\alpha) + 2\mu_s\xi_1(X_1 - X_2)(i\alpha) + X_1 + \lambda_s(X_1 - X_2) + \lambda_d X_d = -\dfrac{\ddot{X}_g}{\omega_1^2} \\ \beta_2 X_2(i\alpha)^2 + 2\mu_2\xi_1 X_2(i\alpha) + 2\mu_s\xi_1(X_2 - X_1)(i\alpha) + \lambda_2 X_2 + \lambda_s(X_2 - X_1) = -\dfrac{\beta_2\ddot{X}_g}{\omega_1^2} \\ \beta_d(X_1 - X_d)(i\alpha)^2 + 2\beta_d\xi_d f_d(X_1 - X_d)(i\alpha) - \lambda_d X_d = -\dfrac{\beta_d\ddot{X}_g}{\omega_1^2} \end{cases} \tag{6}$$

3.2 Solution of the Transfer Function

Before H_2 optimization, it is necessary to obtain the normalized displacement transfer functions of the left structure and the right structure under different connection modes of TID. Solve Eqs. (4) and (6) to obtain the following results.

3.2.1 Serial TID

(1) Left structure

$$X_1^s = \frac{X_1(i\alpha)}{\ddot{X}_g(i\alpha)/\omega_1^2} = -\frac{B_4^s(i\alpha)^4 + B_3^s(i\alpha)^3 + B_2^s(i\alpha)^2 + B_1^s(i\alpha) + B_0^s}{A_6^s(i\alpha)^6 + A_5^s(i\alpha)^5 + A_4^s(i\alpha)^4 + A_3^s(i\alpha)^3 + A_2^s(i\alpha)^2 + A_1^s(i\alpha) + A_0^s} \tag{7}$$

where the superscript "s" denotes serial connection, and the subscript "1" denotes the left structure, and its numerator and denominator coefficients are shown in Appendix A.

(2) Right structure

$$X_2^s = \frac{X_2(i\alpha)}{\ddot{X}_g(i\alpha)/\omega_1^2} = -\frac{C_4^s(j\alpha)^4 + C_3^s(j\alpha)^3 + C_2^s(j\alpha)^2 + C_1^s(j\alpha) + C_0^s}{A_6^s(i\alpha)^6 + A_5^s(i\alpha)^5 + A_4^s(i\alpha)^4 + A_3^s(i\alpha)^3 + A_2^s(i\alpha)^2 + A_1^s(i\alpha) + A_0^s} \tag{8}$$

where the superscript "s" denotes serial connection, the subscript "2" denotes the right structure, the denominator coefficient is the same as the left structure, and the numerator coefficient is shown in Appendix B.

3.2.2 Parallel TID

(1) Left structure

$$X_1^p = \frac{X_1(i\alpha)}{\ddot{X}_g(i\alpha)/\omega_1^2} = -\frac{B_4^p(i\alpha)^4 + B_3^p(i\alpha)^3 + B_2^p(i\alpha)^2 + B_1^p(i\alpha) + B_0^p}{A_6^p(i\alpha)^6 + A_5^p(i\alpha)^5 + A_4^p(i\alpha)^4 + A_3^p(i\alpha)^3 + A_2^p(i\alpha)^2 + A_1^p(i\alpha) + A_0^p} \tag{9}$$

where the superscript "p" denotes parallel connection, the subscript "1" denotes the left structure, and its numerator and denominator coefficients are shown in Appendix C.

(2) Right structure

$$X_2^p = \frac{X_2(i\alpha)}{\ddot{X}_g(i\alpha)/\omega_1^2} = -\frac{C_4^s(i\alpha)^4 + C_3^p(i\alpha)^3 + C_2^p(i\alpha)^2 + C_1^p(i\alpha) + C_0^p}{A_6^p(i\alpha)^6 + A_5^p(i\alpha)^5 + A_4^p(i\alpha)^4 + A_3^p(i\alpha)^3 + A_2^p(i\alpha)^2 + A_1^p(i\alpha) + A_0^p} \tag{10}$$

where the superscript "p" denotes parallel connection, the subscript "2" denotes the right structure, the denominator coefficient is the same as the left structure, and the numerator coefficient is shown in Appendix D.

3.3 Parameters Optimization

In order to verify the damping effect of different types of TID coupled with adjacent buildings, H_2 optimization method is used to optimize the parameters of vibration control system, and the external excitation used in this paper is white noise excitation. If the evaluation index is defined as PI, the H_2 optimization problem can be expressed as the optimization of the corresponding variance. The form of evaluation index PI is:

$$PI = \frac{1}{2\pi}\int_{-\infty}^{\infty}\left|\frac{X(i\alpha)}{\ddot{X}_g(i\alpha)/\omega^2}\right| d\alpha \tag{11}$$

where $\dfrac{X(i\alpha)}{\ddot{X}_g(i\alpha)/\omega^2}$ is the normalized transfer function.

To simplify the analysis, take the damping between the left structure and the right structure as 0, that is, from Table 1: $\xi_1 = 0$, $\mu_2 = 0$, $\mu_s = 0$. After solving the normalized transfer function, the parameters of the left structure and the right structure can be optimized for adjacent buildings with different types of TID coupling.

3.3.1 Optimization Process

(1) Serial TID

After substituting Eqs. (7) and (8) into the evaluation index PI of Eq. (11), using the formula in Appendix E, the evaluation index PI are calculated as follows:

$$PI_1^s = \frac{1}{f_d\xi_d}\left(\frac{Q_1^s}{P_1^s}\lambda_d^2 - \frac{Q_2^s}{P_2^s}\lambda_d + \frac{Q_3^s}{P_3^s}\right) + \frac{f_d\xi_d Q_4^s}{P_4^s} \tag{12}$$

$$PI_2^s = \frac{1}{f_d\xi_d}\left(\frac{N_1^s}{M_1^s}\lambda_d^2 - \frac{N_2^s}{M_2^s}\lambda_d + \frac{N_3^s}{M_3^s}\right) + \frac{f_d\xi_d N_4^s}{M_4^s} \tag{13}$$

where the superscript "s" denotes serial connection, the subscripts "1, 2" denote the left structure and the right structure, respectively. P_n^s $(n = 1,2,3,4)$, Q_n^s $(n = 1,2,3,4)$, M_n^s $(n = 1,2,3,4)$ and N_n^s $(n = 1,2,3,4)$ are polynomials composed of β_d, β_2, λ_2 and λ_s, respectively, see Appendix F and Appendix G for the specific form.

(2) Parallel TID

After substituting Eqs. (9) and (10) into the evaluation index PI of Eq. (11), using the formula in Appendix E, the evaluation index PI are calculated as follows:

$$PI_1^p = \frac{f_d\xi_d Q_1^p}{\lambda_d^2} + \frac{1}{f_d\xi_d}\left(\frac{Q_2^p}{4\lambda_d} + \frac{Q_3^p}{4\lambda_d^2} + \frac{Q_4^p}{P_1^p}\right) \tag{14}$$

$$PI_2^p = f_d\xi_d\left(\frac{N_1^p}{\lambda_d^2 M_1^p} + \frac{N_2^p}{\lambda_d M_2^p} + \frac{N_3^p}{M_2^p}\right) + \frac{1}{f_d\xi_d}\left(\frac{N_4^p}{\lambda_d^2 M_3^p} + \frac{N_5^p}{\lambda_d M_4^p} + \frac{N_6^p}{M_5^p}\right) \tag{15}$$

where the superscript "p" denotes parallel connection, the subscripts "1, 2" denote the left structure and the right structure, respectively. P_1^p, Q_n^p $(n = 1,2,3,4)$, M_n^P $(n = 1,2,3,4,5)$ and N_n^p $(n = 1,2,3,4,5,6)$ are polynomials composed of β_d, β_2, λ_2 and λ_s, respectively, see Appendix H and Appendix I for the specific form.

3.3.2 Optimization Results

In order to obtain the optimum solutions, the evaluation index PI is used to calculate the partial derivatives of the optimization parameters respectively, and make them equal to 0. The following results are obtained:

(1) Serial TID

$$\frac{\partial PI_1^s}{\partial f_d}=0,\ \frac{\partial PI_1^s}{\partial \xi_d}=0,\ \frac{\partial PI_1^s}{\partial \lambda_d}=0 \tag{16}$$

$$\frac{\partial PI_2^s}{\partial f_d}=0,\ \frac{\partial PI_2^s}{\partial \xi_d}=0,\ \frac{\partial PI_2^s}{\partial \lambda_d}=0 \tag{17}$$

By solving Eqs. (16) and (17), respectively, we can get the optimization results (Eq. (18) represents the left structure, and Eq. (19) represents the right structure):

$$\begin{cases}\xi_{dopt1}^s=\dfrac{\sqrt{P_4^s(4(P_2^s)^2Q_1^sQ_3^s-P_1^sP_3^s(Q_2^s)^2)}}{2P_2^s\sqrt{P_3^sQ_1^sQ_4^s}\sqrt{\lambda_{dopt1}^s/\beta_d}}\\ \lambda_{dopt1}^s=\dfrac{P_1^sQ_2^s}{2P_2^sQ_1^s}\end{cases} \tag{18}$$

$$\begin{cases}\xi_{dopt2}^s=\dfrac{\sqrt{M_4^s(4(M_2^s)^2N_1^sN_3^s-M_1^sM_3^s(N_2^s)^2)}}{2M_2^s\sqrt{M_3^sN_1^sN_4^s}\sqrt{\lambda_{dopt2}^s/\beta_d}}\\ \lambda_{dopt2}^s=\dfrac{M_1^sN_2^s}{2M_2^sN_1^s}\end{cases} \tag{19}$$

Here, it is necessary to point out:

$$f_d=\sqrt{\frac{\lambda_d}{\beta_d}} \tag{20}$$

(2) Parallel TID

$$\frac{\partial PI_1^p}{\partial f_d}=0,\ \frac{\partial PI_1^p}{\partial \xi_d}=0,\ \frac{\partial PI_1^p}{\partial \lambda_d}=0 \tag{21}$$

$$\frac{\partial PI_2^p}{\partial f_d}=0,\ \frac{\partial PI_2^p}{\partial \xi_d}=0,\ \frac{\partial PI_2^p}{\partial \lambda_d}=0 \tag{22}$$

By solving Eq. (21) and by Eq. (20), we can get the optimization results of the left structure under the parallel TID coupling are:

$$\begin{cases}\xi_{dopt1}^p=\sqrt{\dfrac{3P_1^pQ_1^p(Q_2^p)^2-\sqrt{P_1^p(Q_1^p)^2(Q_2^p)^2(9P_1^p(Q_2^p)^2-128Q_3^pQ_4^p)}-32Q_1^pQ_3^pQ_4^p}{128(Q_1^p)^2Q_4^p(\lambda_{dopt1}^p/\beta_d)}}\\ \lambda_{dopt1}^p=\dfrac{\sqrt{P_1^p(Q_1^p)^2(Q_2^p)^2(9P_1^p(Q_2^p)^2-128Q_3^pQ_4^p)}}{16Q_1^pQ_2^pQ_4^p}-\dfrac{3P_1^pQ_2^p}{16Q_4^p}\end{cases} \tag{23}$$

When solving Eq. (22), this equation group is converted into the solution of Eq. (24), which includes:

$$\begin{cases} \psi_d \left(R_1\lambda_d^2 + R_2\lambda_d + R_3\right) - R_4\lambda_d^2 - R_5\lambda_d - R_6 = 0 \\ \psi_d \left(R_7\lambda_d - R_8\right) - R_9\lambda_d - R_{10} = 0 \end{cases} \tag{24}$$

where

$$\psi_d = (f_d\xi_d)^2 \tag{25}$$

see Appendix J for the specific form of R_n $(n = 1, 2, \ldots, 10)$.

By solving Eq. (24), and with Eq. (20), the optimization results of the right structure under parallel TID coupling are obtained as follows:

$$\begin{cases} \xi_{dopt2}^p = \sqrt{\dfrac{R_9\lambda_{dopt2}^p + R_{10}}{(R_7\lambda_{dopt2}^p - R_8)(\lambda_{dopt2}^p/\beta_d)}} \\ \lambda_{dopt2}^p = \dfrac{1}{U_1}\left(U_2 + \sqrt[3]{2}\left(1 + i\sqrt{3}\right)\left(U_3 + \sqrt{U_4}\right)^{\frac{1}{3}} - 2i\sqrt[3]{2}\left(i + \sqrt{3}\right)U_5\left(U_3 + \sqrt{U_4}\right)^{-\frac{1}{3}}\right) \end{cases} \tag{26}$$

where U_n (n = 1,2,3,4) is a polynomial composed of R_n $(n = 1, 2, \ldots, 10)$. See Appendix K for the specific form.

4 Parameters Analysis

4.1 Parameters Determination

Before parameters analysis, it is necessary to give specific values of parameters that have not been optimized. In order to facilitate the optimization analysis, the mass, damping and stiffness of the left structure and the right structure are determined to be consistent in this section, that is, Table 1 shows: $\beta_2 = 1.0$, $\lambda_2 = 1.0$. In the following analysis, we first determine the mass ratio β_d and the stiffness ratio λ_s, and then conduct relevant parameters analysis.

4.1.1 Determination of β_d

In Section 3.3.2, the process and results of parameter optimization are given. However, many of the optimization results have root signs. According to the mathematical knowledge, all values under the root sign should be greater than or equal to 0. After considering all the optimization results, it is found that the conditions affecting the value of β_d are shown in Eq. (27):

$$9P_1^p(Q_2^p)^2 - 128Q_3^pQ_4^p \geq 0 \tag{27}$$

To determine the value of β_d, let the left side of inequality (27) be 0, that is, there is Eq. (28):

$$\gamma = 9P_1^p(Q_2^p)^2 - 128Q_3^pQ_4^p = 0 \tag{28}$$

Combining Eqs. (H1) and (H2), the image of Eq. (28) is drawn as shown in Fig. 4. It can be seen from the figure that if $\gamma \geq 0$, the value of β_d should be between 0 and 0.244. Considering that the value of β_d is often small in real life, we can temporarily take the mass ratio $\beta_d = 0.1$ for the next analysis.

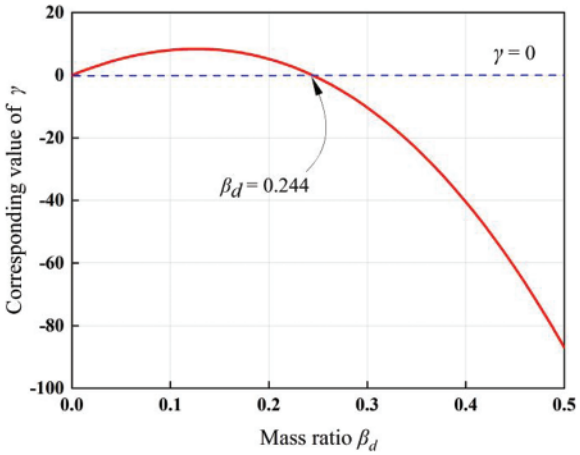

Figure 4: Analysis of the value of mass ratio β_d

4.1.2 Determination of λ_s

It was found during parameter optimization that if λ_s is the parameter to be optimized, the equation set could not be solved. So, the determination of λ_s in advance is a key problem, and it is also a different point and difficulty in dealing with the vibration control of adjacent buildings. In the actual project, k_s is generally less than the stiffness of the left structure k_1. Therefore, it can be determined in advance that the value range of λ_s is 0.1∼0.7. The determination of β_d has been given in Section 4.1.1, and the value is 0.1. According to the above conditions, we can get the function of normalized displacement, which only contains normalized frequency α and stiffness ratio λ_s. The two parameters, then, can draw a three-dimensional graph for analysis, and then determine the value of λ_s. Fig. 5 shows a three-dimensional graph of normalized displacement under different conditions, considering different values of λ_s. In Fig. 5, α is between 0 and 2, and λ_s is between 0.1 and 0.7.

As can be seen from Fig. 5, when λ_s takes different values, the normalized displacement graph of the left structure coupled with two connection modes TID is similar (Figs. 5a and 5c), and the normalized displacement graph of the right structure is also similar (Figs. 5b and 5d). The peak value of the normalized displacement (for the convenience of description, the peak value of the displacement transfer function graph is called the wave peak) shows that for the left structure, the value of λ_s does not affect the number of wave peaks. But for the right structure, when $\lambda_s \leq 0.3$ or so, the number of wave peaks will degenerate into two. It can also be seen from Fig. 5 that when $\lambda_s \leq 0.2$, the normalized displacement will increase sharply, while when λ_s is between 0.2 and 0.7, the displacement image tends to be stable and at a low level. In order to facilitate the next research, and considering the better damping performance of the system when λ_s is large and the constraints of the actual engineering structure, it is decided to set λ_s as 0.5.

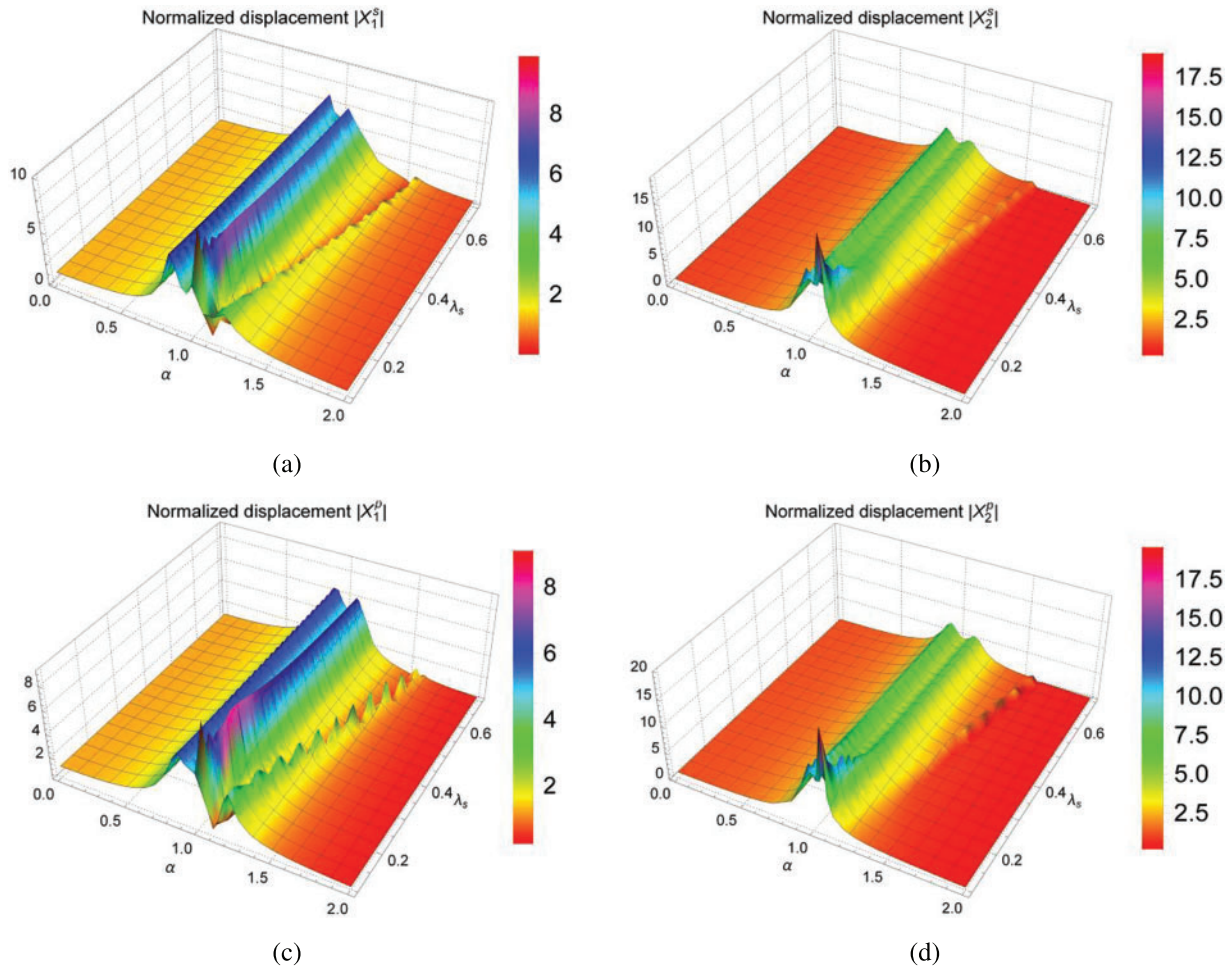

Figure 5: Three-dimensional graphs of normalized displacement when the stiffness ratio λ_s take different values: (a) The left structure under serial TID coupling; (b) The right structure under serial TID coupling; (c) The left structure under parallel TID coupling; (d) The right structure under parallel TID coupling

4.1.3 Verification of Optimization Results

After the values of two key parameters β_d and λ_s are determined, they can be substituted into the optimization result equations under different conditions, and the values of the optimum solutions λ_{dopt} and ξ_{dopt} can be obtained. At the same time, according to the evaluation index PI (Eqs. (12)–(15)) given earlier, a three-dimensional graph of PI (Fig. 6) can be drawn, and the accuracy of the optimization results can be verified.

It can be seen from Figs. 6a and 6b that the evaluation indexes PI of the left structure and the right structure under the serial TID coupling are similar, the lowest point appears near $\lambda_d = 0.09\sim0.11$ and $\xi_d = 0.10\sim0.14$. For the three-dimensional graph of evaluation index PI of left structure and right structure under the coupling of parallel TID, it can be seen from Figs. 6c and 6d that when $\lambda_d \geq 0.28$ and $\xi_d \geq 0.3$, the value of PI_1^p in three-dimensional graph is relatively stable and the minimum value of PI cannot be obtained within this range, but when $\lambda_d = 0.10\sim0.11$ and $\xi_d = 0.11\sim0.15$, PI_1^p can get

the minimum value. Similarly, when $\lambda_d = 0.11 \sim 0.13$ and $\xi_d = 0.10 \sim 0.13$, PI_2^p can get the minimum value. In order to further determine the values of λ_d and ξ_d, the contour graphs are drawn in detail as shown in Fig. 7.

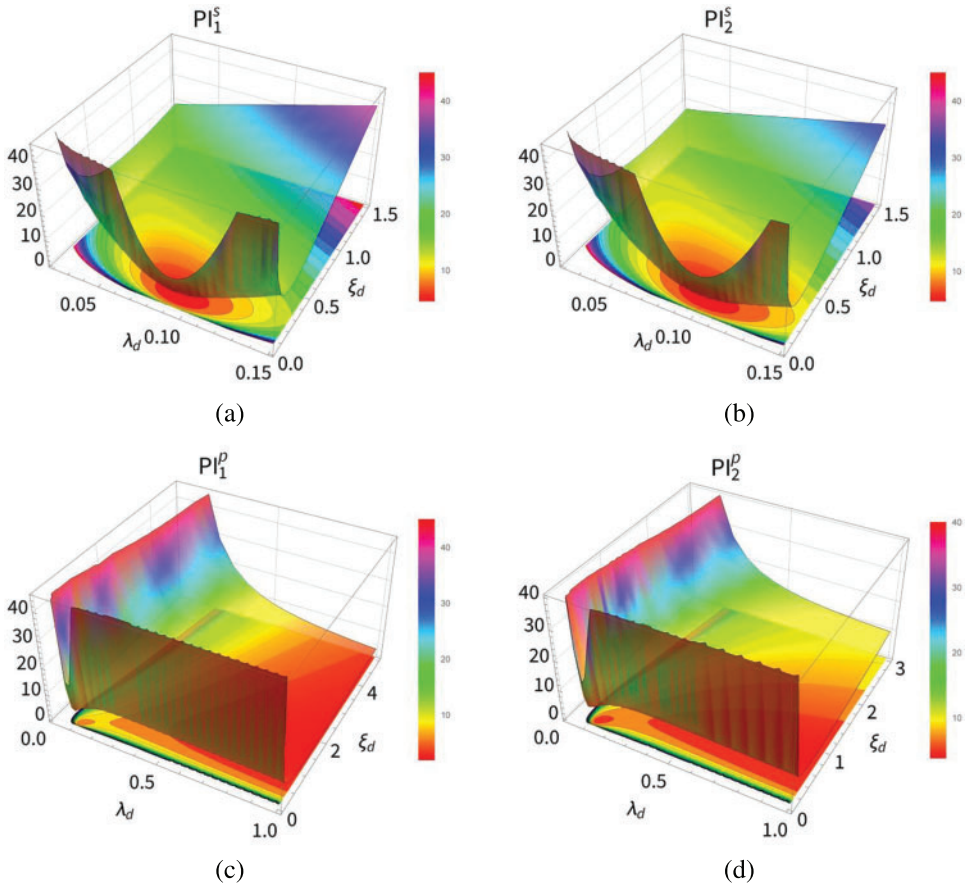

Figure 6: Three-dimensional graphs of evaluation index PI by H_2 optimization method (λ_d is the ratio of stiffness of TID to stiffness of left structure, ξ_d is the nominal damping ratio of TID): (a) The left structure under serial TID coupling; (b) The right structure under serial TID coupling; (c) The left structure under parallel TID coupling; (d) The right structure under parallel TID coupling

From the closure of the contour graphs in Figs. 6 and 7, we can roughly judge the coordinates when $PI = 0$, and the results are listed in Table 2. As mentioned above, the calculated value of the optimum solutions can be obtained by substituting the previously determined parameters: $\beta_2 = 1.0$, $\lambda_2 = 1.0$, $\lambda_s = 0.5$ and $\beta_d = 0.1$ into Eqs. (18), (19), (23) and (26), and the results are shown in Table 2. As can be seen from Table 2, compared with the calculated value of the optimum solutions, the error of the predicted optimum solutions from Fig. 7 is small, and the maximum error is only 3.31%. Therefore, the optimization results obtained by the process in Section 3 are accurate. Due to the error in the estimated value obtained through figure judgment, the calculated values are used for the optimum solution during subsequent analysis.

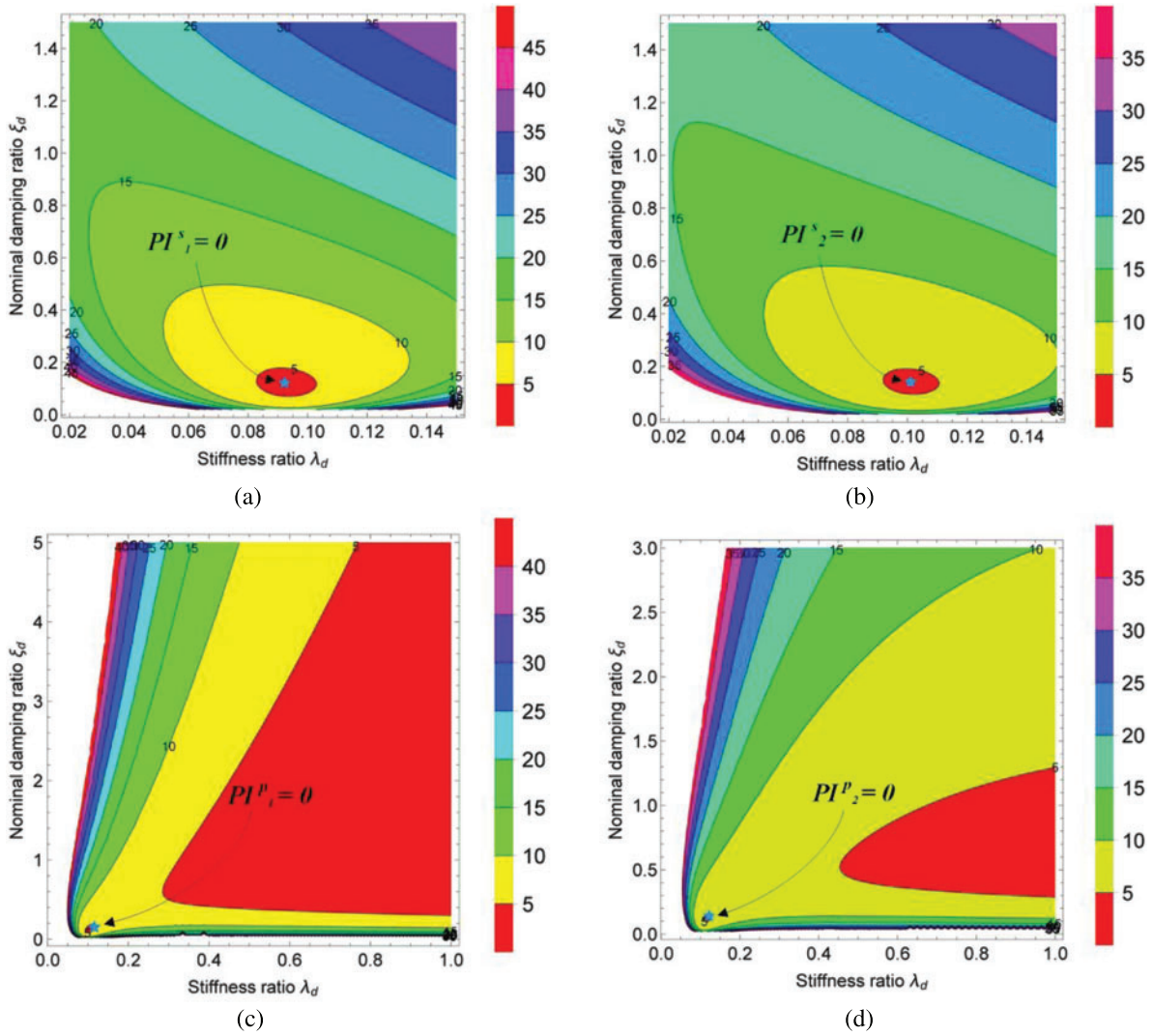

Figure 7: The contour graphs of evaluation index PI of H_2 optimization method (a, b, c and d correspond to Fig. 6). The blue pentagram marks the point where $PI = 0$, and its corresponding λ_d and ξ_d are the optimum solutions λ_{dopt} and ξ_{dopt}

Table 2: Comparison between the estimated values and the calculated values of the optimum solutions

Connection modes	Structure types	Estimated values		Calculated values		Error rate (%)	
		$\lambda_{dopt}{}^e$	$\xi_{dopt}{}^e$	λ_{dopt}	ξ_{dopt}	Δ_λ	Δ_ξ
Serial TID	Left structure	0.094	0.110	0.093	0.111	1.08	0.90
	Right structure	0.102	0.135	0.101	0.134	0.99	0.75
Parallel TID	Left structure	0.103	0.125	0.103	0.121	0.00	3.31
	Right structure	0.118	0.123	0.116	0.120	1.72	2.50

4.2 Influence of Parameters on Optimum Solutions

In 1998, Rana et al. put forward that the frequency ratio is an important index that affects the damping performance when designing TMD through the fixed-points theory [49]. Considering the impact of actual engineering on the optimum solution results is conducive to further understanding the laws of TID for vibration control of adjacent building structures. The influence of different parameters on the optimum solution is analyzed as follows:

4.2.1 Influence of Mass Ratios β_d and β_2

Figs. 8 and 9 are three-dimensional graphs of optimum solutions f_{dopt} and ξ_{dopt} of left structure and right structure under the coupling of serial TID and parallel TID, respectively. Figs. 10 and 11 are two-dimensional graphs corresponding to Figs. 8 and 9, respectively.

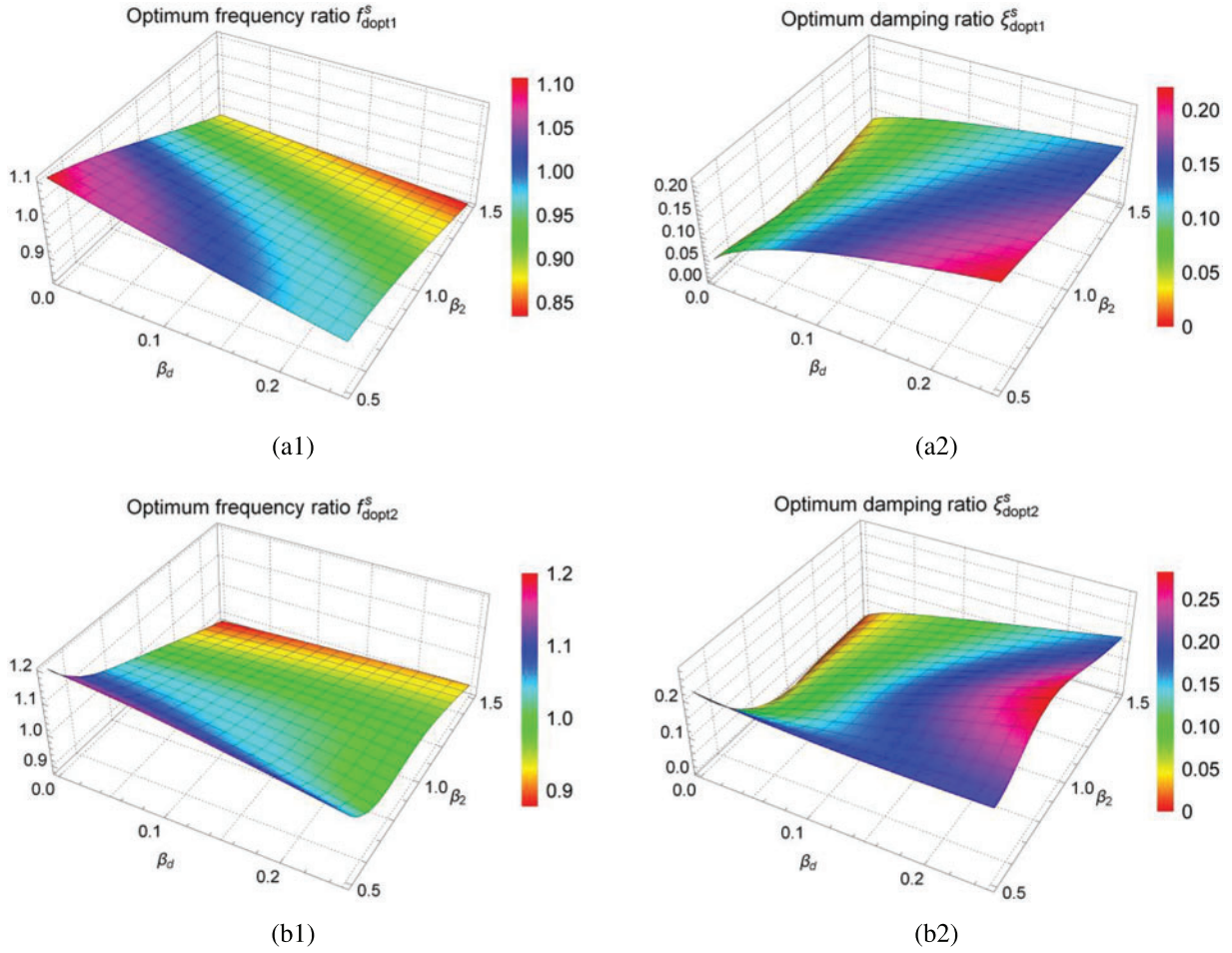

(a1) (a2)

(b1) (b2)

Figure 8: Three-dimensional graphs of optimum solutions f_{dopt} and ξ_{dopt} under serial TID coupling ($\lambda_2 = 1.0$, $\lambda_s = 0.5$). In the figure, (a1) and (a2) correspond to the left structure, and (b1) and (b2) correspond to the right structure

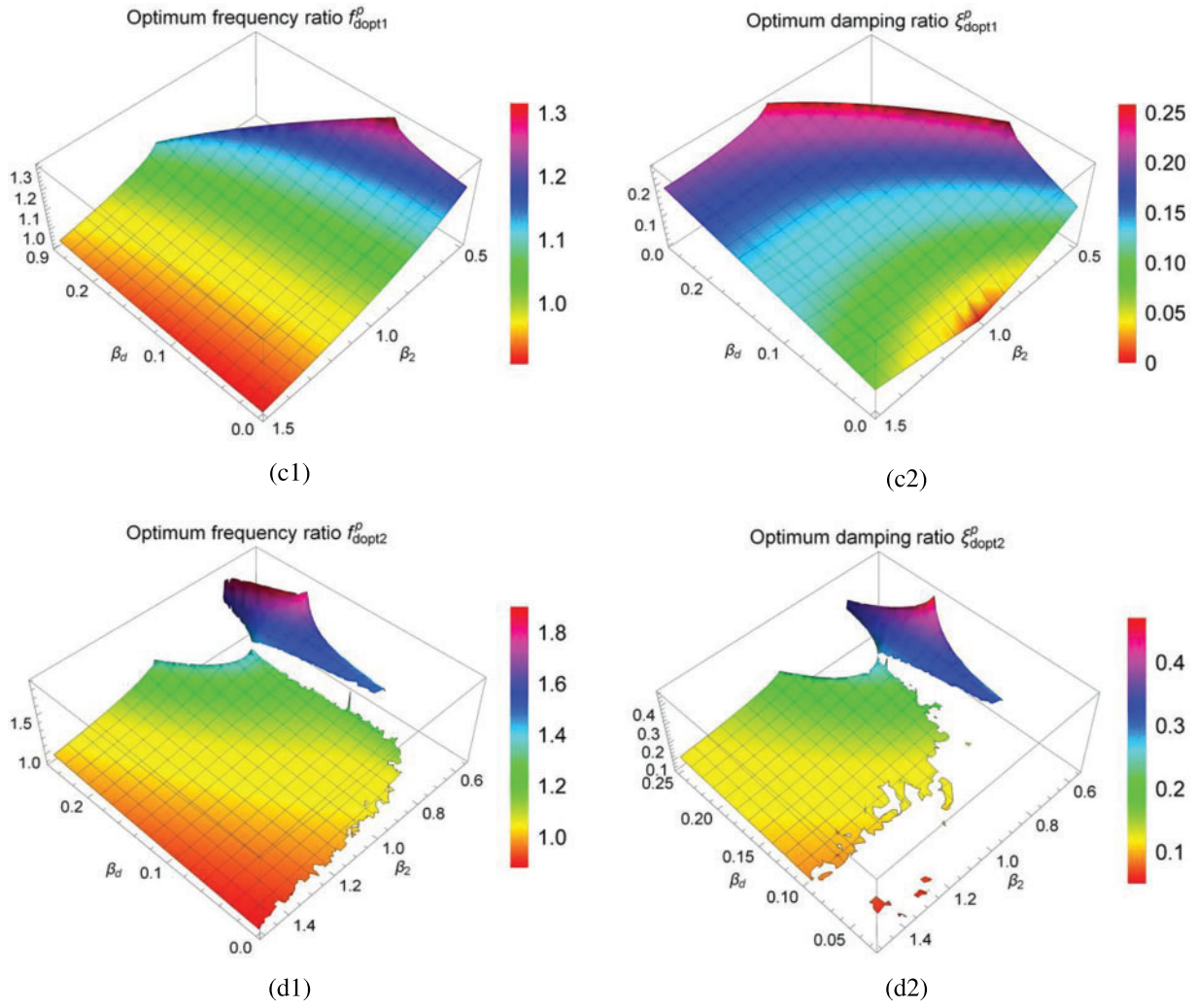

Figure 9: Three-dimensional graphs of optimum solutions f_{dopt} and ξ_{dopt} under parallel TID coupling ($\lambda_2 = 1.0$, $\lambda_s = 0.5$). In the figure, (c1) and (c2) correspond to the left structure, and (d1) and (d2) correspond to the right structure

In Figs. 8(a1) and 8(a2), the optimum frequency ratio f_{dopt} of the left structure under serial TID coupling decreases with the increase of mass ratio β_d, while the optimum damping ratio ξ_{dopt} increases with the increase of mass ratio β_d. It can be seen from Fig. 10(a1) that when β_2 is small, f_{dopt} decreases rapidly, and with the increase of β_2, f_{dopt} decreases more and more slowly. In Fig. 10(a2), the value of β_2 has little effect on the rising speed of ξ_{dopt}. In Figs. 8(b1), and 8(b2), for the right structure coupled by serial TID, β_2 has obvious influence on f_{dopt} and ξ_{dopt}. When β_2 is small, both f_{dopt} and ξ_{dopt} decrease with the increase of mass ratio β_d; While when β_2 is larger, both f_{dopt} and ξ_{dopt} increase with the increase of β_d. The above results show that the mass ratio β_2 has a great influence on the right structure in the adjacent building structures coupled by serial TID. In order to achieve the best control effect, with the increase of β_d, the required spring stiffness k_d decreases and the damping c_d increases for the left structure. However, for the right structure, when the mass ratio β_2 is small, with the increase of β_2,

the required spring stiffness k_d and damping c_d become smaller and smaller. When the mass ratio β_2 is large, with the increase of β_2, the required spring stiffness k_d and damping c_d become larger and larger.

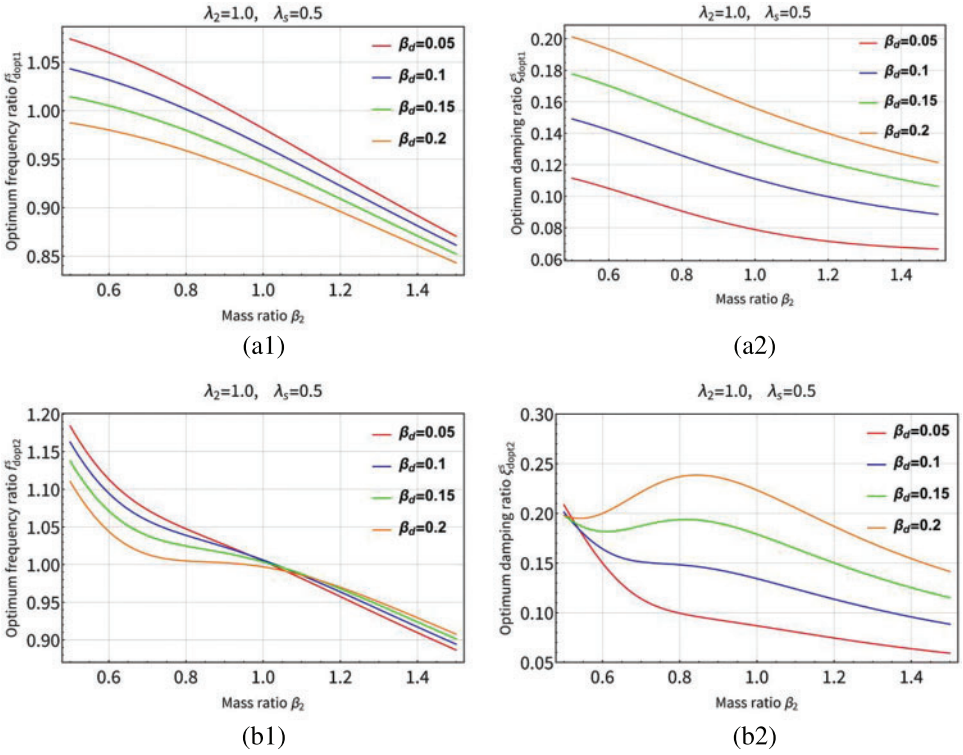

Figure 10: The curves of the optimum solutions (f_{dopt}, ξ_{dopt}) of the left structure and the right structure under the coupling of serial TID when β_d takes different values (a and b correspond to Figs. 8a and 8b)

Under parallel TID coupling, it can be seen from Fig. 9 that the f_{dopt} and ξ_{dopt} of the left structure and the right structure both increase with the increase of β_d. According to the observation in Fig. 11, when β_2 is small, f_{dopt} and ξ_{dopt} increase rapidly, while when β_2 is large, the increasing trend of f_{dopt} and ξ_{dopt} slows down. Therefore, the mass ratio β_2 has obvious influence on both the left structure and the right structure, and the influence trends are the same. For the left structure and the right structure, in order to achieve the best control effect, with the increase of β_d, the required spring stiffness k_d and damping c_d become larger and larger, and the larger β_2 is, the slower the increase speed is.

4.2.2 Influence of Stiffness Ratios λ_s and λ_2

Figs. 12 and 13 are three-dimensional graphs of optimum solutions f_{dopt} and ξ_{dopt} of left structure and right structure under the coupling of serial TID and parallel TID, respectively. Figs. 14 and 15 are two-dimensional graphs corresponding to Figs. 12 and 13, respectively.

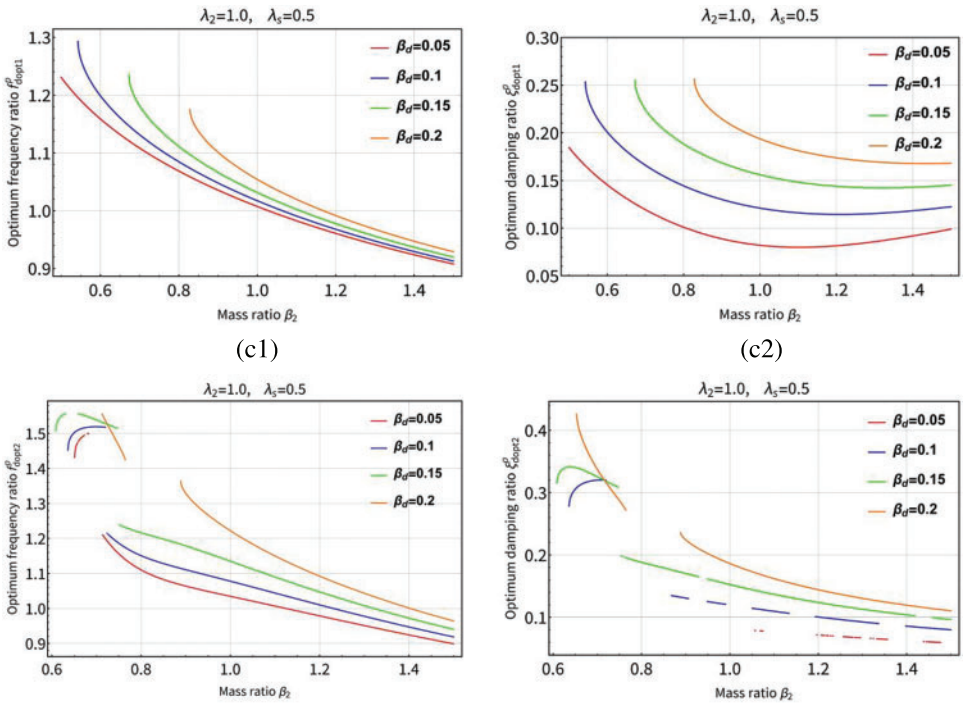

Figure 11: The curves of the optimum solutions (f_{dopt}, ξ_{dopt}) of the left structure and the right structure under the coupling of parallel TID when β_d takes different values (c and d correspond to Figs. 9c and 9d)

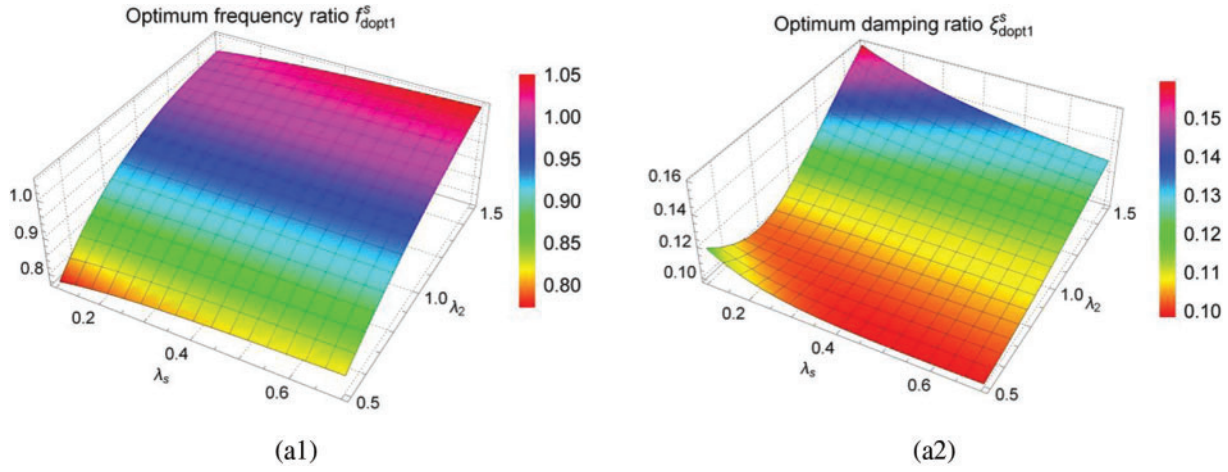

Figure 12: (Continued)

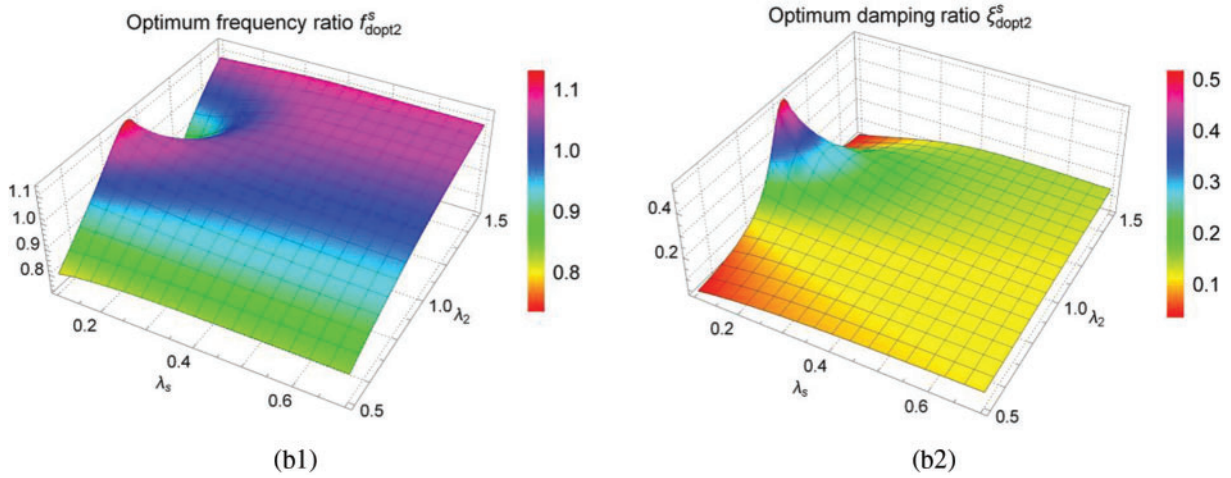

Figure 12: Three-dimensional graphs of the optimum solutions f_{dopt} and ξ_{dopt} under serial TID coupling ($\beta_d = 0.1$, $\beta_2 = 1.0$). In the figure, (a1) and (a2) correspond to the left structure, and (b1) and (b2) correspond to the right structure

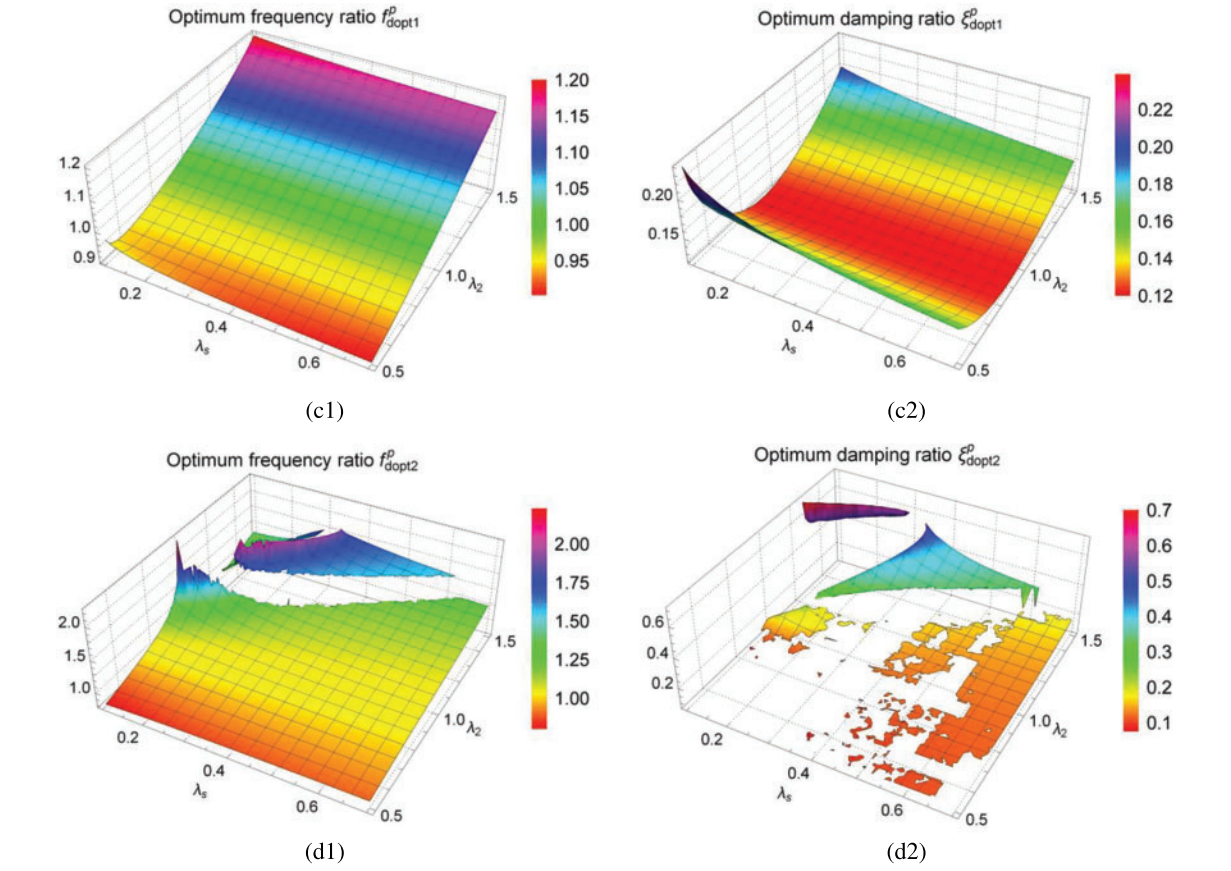

Figure 13: Three-dimensional graphs of the optimum solutions f_{dopt} and ξ_{dopt} under parallel TID coupling ($\beta_d = 0.1$, $\beta_2 = 1.0$). In the figure, (c1) and (c2) correspond to the left structure, and (d1) and (d2) correspond to the right structure

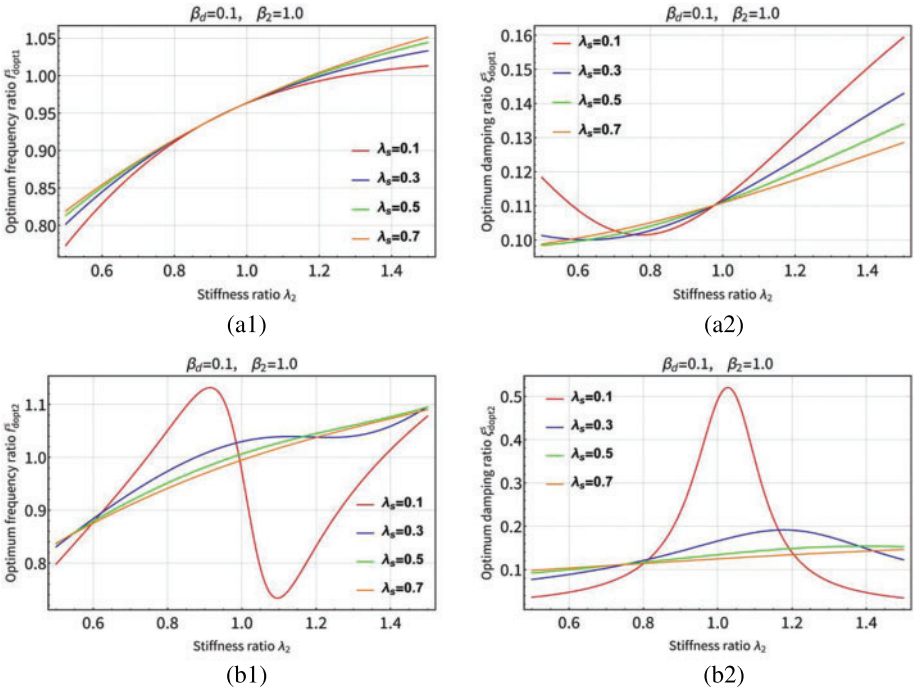

Figure 14: The curves of the optimum solutions (f_{dopt}, ξ_{dopt}) of the left structure and the right structure under the coupling of serial TID when λ_s takes different values (a and b correspond to Figs. 12a and 12b)

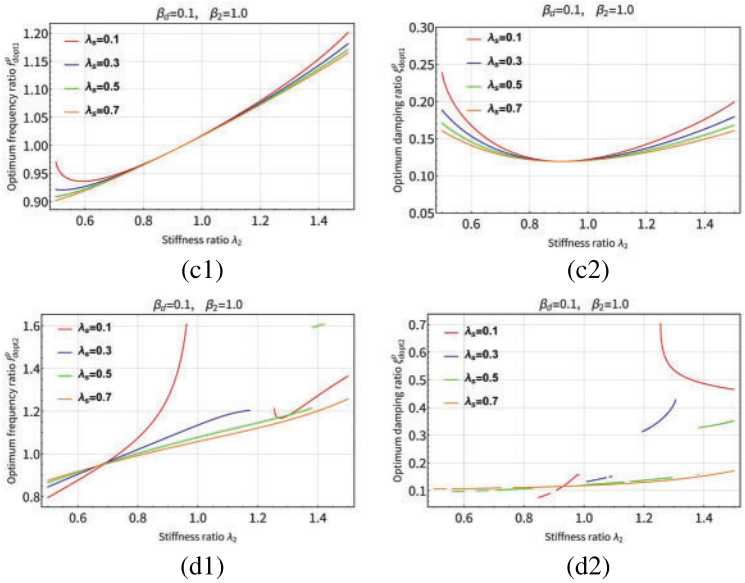

Figure 15: The curves of the optimum solutions (f_{dopt}, ξ_{dopt}) of the left structure and the right structure under the coupling of parallel TID when λ_s takes different values (c and d correspond to Figs. 13c and 13d)

For the adjacent buildings coupled by serial TID, it can be seen from Figs. 12, 14(a1) and 14(a2) that the optimum frequency ratio f_{dopt} of the left structure increases with the increase of stiffness ratio λ_2, and it is not obviously affected by stiffness ratio λ_s. The optimum damping ratio ξ_{dopt} is obviously affected by the stiffness ratio λ_s. When λ_s is small, ξ_{dopt} first decreases and then increases with the increase of λ_2, while when λ_s is large, ξ_{dopt} always increases with the increase of λ_2. The above results show that, in order to achieve the best control effect, with the increase of stiffness ratio λ_s and λ_2, the required stiffness provided by TID will be larger for the left structure coupled with serial TID. As for damping, when λ_s is small, with the increase of λ_2, the damping provided by TID decreases first and then increases; when λ_s is large, with the increase of λ_s, the damping required by TID is larger. It can be seen from Figs. 12, 14(b1) and 14(b2) that the optimum frequency ratio f_{dopt} and the best damping ratio ξ_{dopt} of the right structure are significantly affected by the stiffness ratio λ_s. When λ_s is small ($\lambda_s \leq 0.3$), f_{dopt} increases first and then decreases and then increases with the increase of stiffness ratio λ_2, and ξ_{dopt} increases first and then decreases with the increase of stiffness ratio λ_2. When λ_s is larger ($0.3 < \lambda_s \leq 0.7$), both f_{dopt} and ξ_{dopt} increase with the increase of stiffness ratio λ_2, and the increasing speed is relatively slow. The above results show that, in order to achieve the best control effect, when λ_s is small, with the increase of λ_2, the stiffness provided by TID increases first and then decreases and then increases, and the required damping increases first and then decreases. When λ_s is larger, the larger λ_2 is, the greater the stiffness and damping that TID needs to provide.

For adjacent buildings with parallel TID coupling, it can be seen from Figs. 13, 15(c1) and 15(c2) that the optimum frequency ratio f_{dopt} of the left structure is obviously affected by the stiffness ratio λ_s. When λ_s is small, f_{dopt} first decreases and then increases with the increase of λ_2, while when λ_s is larger, f_{dopt} always increases with the increase of λ_2. ξ_{dopt} is not obviously affected by the stiffness ratio λ_s. Under the same stiffness ratio λ_s, ξ_{dopt} decreases with the increase of λ_2. The above results show that, in order to achieve the best control effect, when λ_s is small, with the increase of λ_2, the stiffness provided by TID decreases first and then increases, and the required damping also decreases first and then increases; when λ_s is larger, with the increase of λ_2, the stiffness required by TID is larger, and the required damping also decreases first and then increases. For the right structure, it can be seen from Figs. 13, 15(d1) and 15(d2) that the optimum frequency ratio f_{dopt} and the optimum damping ratio ξ_{dopt} are significantly affected by the stiffness ratio λ_s, similar to the serial TID. When λ_s is small ($\lambda_s \leq 0.3$), f_{dopt} increases first and then decreases and then increases with the increase of stiffness ratio λ_2, and ξ_{dopt} increases first and then decreases with the increase of stiffness ratio λ_2. When λ_s is larger ($0.3 < \lambda_s \leq 0.7$), both f_{dopt} and ξ_{dopt} increase with the increase of stiffness ratio λ_2, and the increasing speed is relatively slow. This shows that, in order to achieve the best control effect, with the change of stiffness ratio λ_s and λ_2, the change trend of required stiffness and damping of the right structure coupled with parallel TID is similar to that of the right structure coupled with serial TID.

5 Frequency Response Analysis

After parameter analysis, we introduce classic tuned mass damper (TMD) into the earthquake resistance of adjacent building structures, and analyze its vibration control performance. Under the condition that all the conditions of the specified structure are unchanged, the vibration control performance of two types of TID and TMD are compared.

5.1 Classic TMD System

5.1.1 Classic TMD Equations

Fig. 16 shows the damping model of adjacent buildings coupled with TMD, which is the same as the definition in Section 3.1. It is defined that the structure on the left side is the left structure and the structure on the right side is the right structure. The mass, damping and stiffness of TMD are m_t, c_t and k_t, respectively. m_1, m_2 are the mass of the left structure and the right structure, respectively, c_1, c_2 and c_s are the damping of the left structure, the right structure and the damping between the left and right structures, respectively, k_1, k_2 and k_s are the stiffness of the left structure, the right structure and the stiffness between the left and right structures, respectively. $\ddot{x}_g$ is the acceleration of seismic waves, and x_1, x_2 and x_t are the displacement of the left structure, right structure and TMD, respectively.

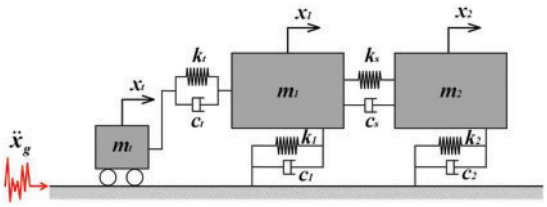

Figure 16: The damping system of adjacent buildings coupled with classic TMD

According to the principle of force balance, the dynamic equilibrium equations are:

$$\begin{cases} m_1\ddot{x}_1 + c_1\dot{x}_1 + c_s(\dot{x}_1 - \dot{x}_2) + c_t(\dot{x}_1 - \dot{x}_t) + k_1x_1 + k_s(x_1 - x_2) + k_t(x_1 - x_t) = -m_1\ddot{x}_g \\ m_2\ddot{x}_2 + c_2\dot{x}_2 + c_s(\dot{x}_2 - \dot{x}_1) + k_2x_2 + k_s(x_2 - x_1) = -m_2\ddot{x}_g \\ m_t\ddot{x}_t + c_t(\dot{x}_t - \dot{x}_1) + k_t(x_t - x_1) = -m_t\ddot{x}_g \end{cases} \tag{29}$$

Using Laplace transform to make dimensionless, and after finishing, get:

$$\begin{cases} X_1(i\alpha)^2 + 2\xi_1X_1(i\alpha) + 2\mu_s\xi_1(X_1 - X_2)(i\alpha) + 2\beta_t\xi_tf_t(X_1 - X_t)(i\alpha) + X_1 + \lambda_s(X_1 - X_2) \\ \quad + \lambda_t(X_1 - X_t) = -\dfrac{\ddot{X}_g}{\omega_1^2} \\ \beta_2X_2(i\alpha)^2 + 2\mu_2\xi_1X_2(i\alpha) + 2\mu_s\xi_1(X_2 - X_1)(i\alpha) + \lambda_2X_2 + \lambda_s(X_2 - X_1) = -\dfrac{\beta_2\ddot{X}_g}{\omega_1^2} \\ \beta_tX_t(i\alpha)^2 + 2\beta_t\xi_tf_t(X_t - X_1)(i\alpha) + \lambda_t(X_t - X_1) = 0 \end{cases} \tag{30}$$

where $\beta_t = m_t/m_1$ is the ratio of the classic TMD mass to the left structure mass, $\xi_t = c_t/2\sqrt{k_tm_t}$ is the nominal damping ratio of classic TMD, $\lambda_t = k_t/k_1$ is the ratio of classic TMD stiffness to left structural stiffness, $f_t = \omega_t/\omega_1$ is the ratio of the nominal frequency of the classic TMD to the frequency of the left structure, X_t is the form of x_t after Laplace transformation. The definitions of other parameters are the same as those in Section 3.1.1, see Table 1.

5.1.2 Optimization Results

Same as the steps in Section 3, the optimization results obtained by H_2 optimization method are as follows:

(1) Left structure

$$\begin{cases} \xi_{topt1} = \dfrac{\sqrt{P_4(4(P_2)^2 Q_1 Q_3 - P_1 P_3 (Q_2)^2)}}{2P_2\sqrt{P_3 Q_1 Q_4}\sqrt{\lambda_{topt1}/\beta_t}} \\ \lambda_{topt1} = \dfrac{P_1 Q_2}{2P_2 Q_1} \end{cases} \tag{31}$$

where P_n ($n = 1,2,3,4$) and Q_n ($n = 1,2,3,4$) are polynomials composed of β_t, β_2, λ_2 and λ_s, respectively, see Appendix L for the specific form.

Similarly, for the classic TMD, there are:

$$f_t = \sqrt{\frac{\lambda_t}{\beta_t}} \tag{32}$$

(2) Right structure

$$\begin{cases} \xi_{topt2} = \dfrac{\sqrt{M_4(4(M_2)^2 N_1 N_3 - M_1 M_3 (N_2)^2)}}{2M_2\sqrt{M_3 N_1 N_4}\sqrt{\lambda_{topt2}/\beta_t}} \\ \lambda_{topt2} = -\dfrac{M_1 N_2}{2M_2 N_1} \end{cases} \tag{33}$$

where M_n ($n = 1,2,3,4$) and N_n ($n = 1,2,3,4$) are polynomials composed of β_t, β_2, λ_2 and λ_s, respectively, see Appendix M for the specific form.

In order to compare the damping performance of two types of TID and classic TMD, this section adopts the parameters determined in Section 4.1, namely $\beta_2 = 1.0$, $\lambda_2 = 1.0$, $\lambda_s = 0.5$. When analyzing the parameters of TID, we take the mass ratio $\beta_d = 0.1$, so when analyzing the damping effect of adjacent buildings under the classic TMD coupling, we also take the mass ratio $\beta_t = 0.1$, and then make the next comparative analysis.

5.2 Comparison of Vibration Control Effect

In the previous analysis, the values of relevant parameters have been determined as follows: $\beta_2 = 1.0$, $\lambda_2 = 1.0$, $\lambda_s = 0.5$, the β_d of adjacent buildings under TID coupling is 0.1, and the β_t of adjacent buildings under classic TMD coupling is also 0.1. The normalized displacement figure under different conditions is shown in Fig. 17.

As can be seen from Fig. 17, the similarity of normalized displacement curves under different conditions is high, and there are three peaks. According to the observation of Fig. 17a, compared with the highest point of the whole curve, the parallel TID value is the smallest; according to the observation of Fig. 17b, compared with the highest point of the whole curve, the classic TMD value is the smallest. The above results show that when damping adjacent buildings, the best control effect can be achieved by selecting parallel TID for the left structure and classic TMD for the right structure. For further comparison, the relevant data of Figs. 17a and 17b are summarized in Table 3. It can be seen from the table that compared with the highest point of displacement curve, the left structure is smaller than the right structure for the adjacent buildings coupled by serial and parallel TIDs, which indicates that TID has better vibration control effect for the left structure. However, for the adjacent buildings coupled with classic TMD, the highest point of the displacement curve of the left structure is larger than that of the right structure, which indicates that the classic TMD has a better damping effect on the right structure. From the results given in Table 3, it can be seen that if the size of the area S (i.e.,

H_2 norm) enclosed by the displacement curve and the coordinate axis in the normalized frequency range of 0∼2.0 is taken as the basis (hereinafter referred to as area S for convenience of analysis), the serial TID has a better vibration control effect for the left structure, and the classic TMD has a better vibration control effect for the right structure.

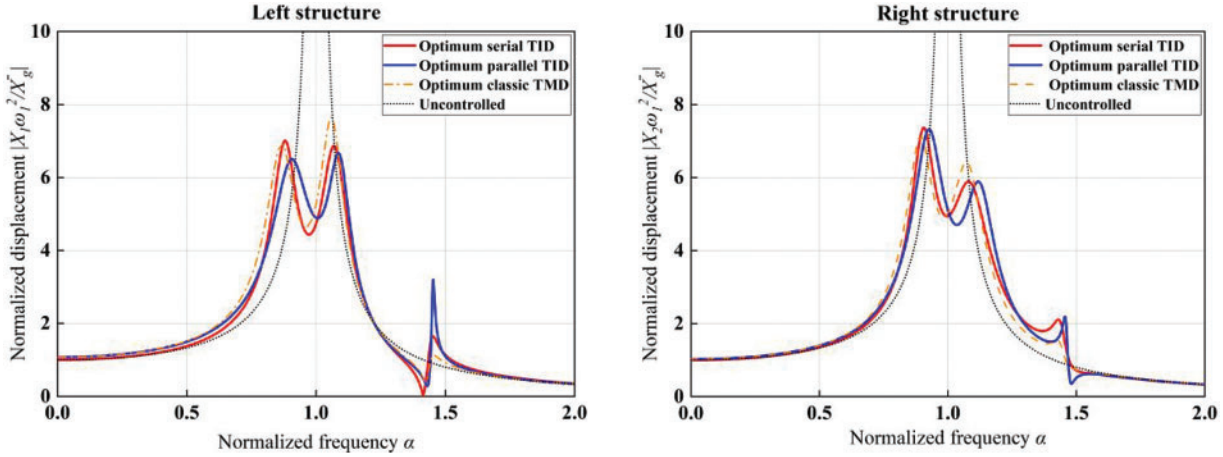

(a) (b)

Figure 17: Normalized displacement graphs of the left structure and right structure of adjacent buildings with different types of dampers ($\beta_2 = 1.0$, $\lambda_2 = 1.0$, $\lambda_s = 0.5$, $\beta_d = 0.1$, $\beta_t = 0.1$)

Table 3: Normalized displacement correlation coefficients of adjacent buildings under different damper coupling

Damper types	Structure types	Peak			Corresponding α			S
		Wave peak 1	Wave peak 2	Wave peak 3	Wave peak 1	Wave peak 2	Wave peak 3	
Serial TID	Left structure	7.007	6.863	1.644	0.880	1.069	1.452	3.907
	Right structure	7.365	5.890	2.109	0.906	1.080	1.430	4.074
Parallel TID	Left structure	6.501	6.668	3.199	0.907	1.086	1.453	4.018
	Right structure	7.323	5.890	2.188	0.926	1.118	1.456	4.108
Classic TMD	Left structure	6.919	7.647	1.127	0.867	1.059	1.454	4.109
	Right structure	7.150	6.431	1.541	0.894	1.072	1.428	4.071

Note: In the table, "S" is the area of the graph enclosed by the normalized displacement curve and coordinate axis (i.e., H_2 norm), and the normalized frequency is $\alpha = 0$∼2.0.

As far as the damping effect of TID is concerned, only the specific case of mass ratio $\beta_d = 0.1$ has been analyzed above, which is obviously not well considered. Fig. 18 is a three-dimensional graph of the normalized displacement of the left structure and the right structure under the coupling of serial TID and parallel TID. From this graph, it can be found that the normalized displacement will gradually decrease with the increase of the mass ratio β_d. For better comparison, the peak value and area S of the displacement curve when β_d takes different values are calculated and summarized in Fig. 19.

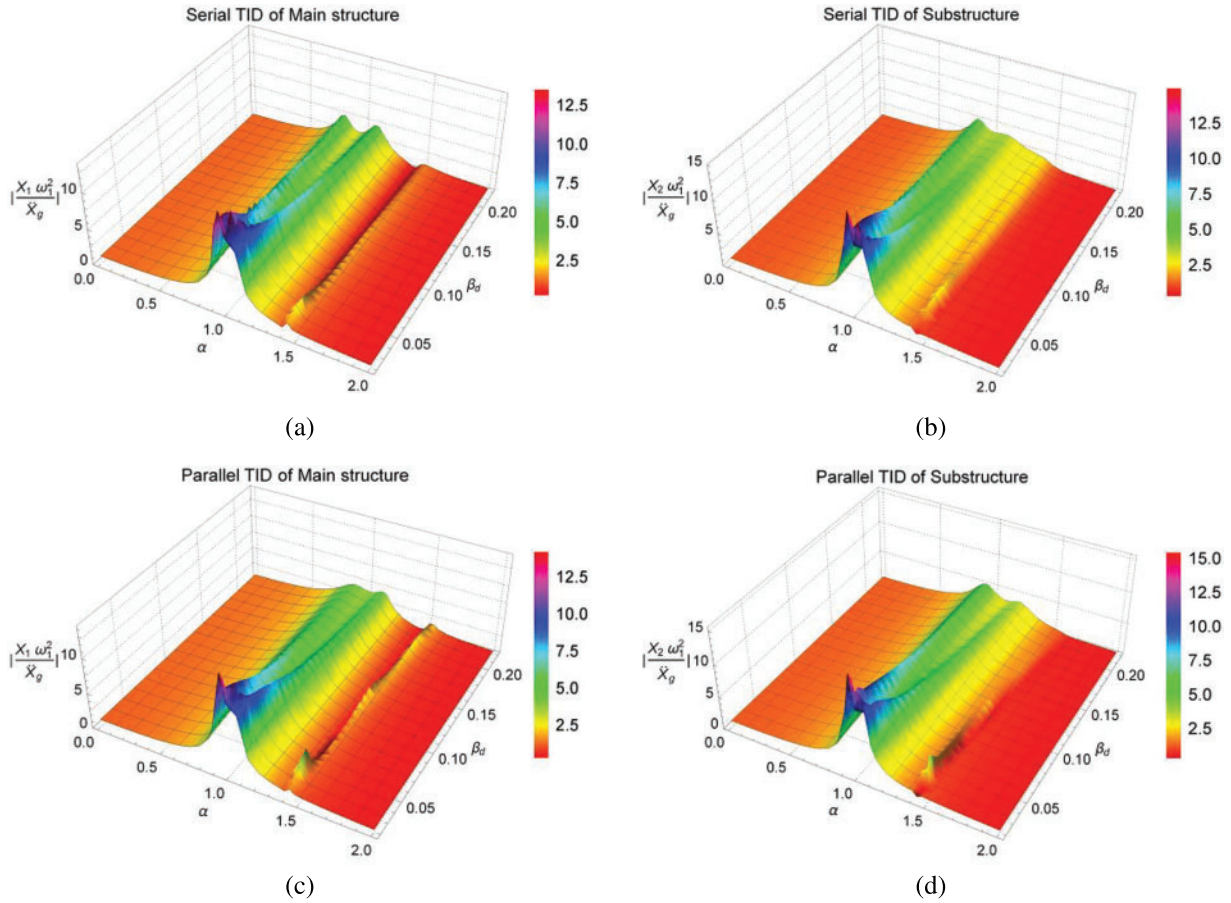

Figure 18: Three-dimensional graphs of normalized displacement when the mass ratio β_d takes different values: (a) The left structure under serial TID coupling; (b) The right structure under serial TID coupling; (c) The left structure under parallel TID coupling; (d) The right structure under parallel TID coupling ($\beta_2 = 1.0$, $\lambda_2 = 1.0$, $\lambda_s = 0.5$)

It can be seen from Fig. 19a that increasing the mass ratio β_d can obviously enhance the damping effect. From the peak value of displacement, when $\beta_d \leq 0.1$, increasing β_d will obviously reduce the peak value of displacement. However, when $\beta_d > 0.1$, the peak value of displacement will decrease more and more slowly. By observing the change of the area S in the bar graph, the height difference between the two bar graphs is also slowly decreasing. According to the line graph and bar graph, it can be found that parallel TID has obvious advantages in controlling the peak displacement, and this advantage becomes greater with the increase of β_d. Comparing the size of area S, it can be seen that serial TID has a significant advantage in controlling the overall vibration control effect, and this advantage increases with the increase of β_d. It can be seen from the line graph and curve graph in Fig. 19b that the value of β_d has the same effect on the peak displacement and area S of the right structure and the left structure. At the same time, for the right structure, the serial TID has a significant advantage in controlling the overall vibration control effect, and this advantage increases with the increase of β_d. However, compared with the peak value of the displacement of the right structure, the serial TID and the parallel TID are similar in size, and the influence of β_d is not obvious.

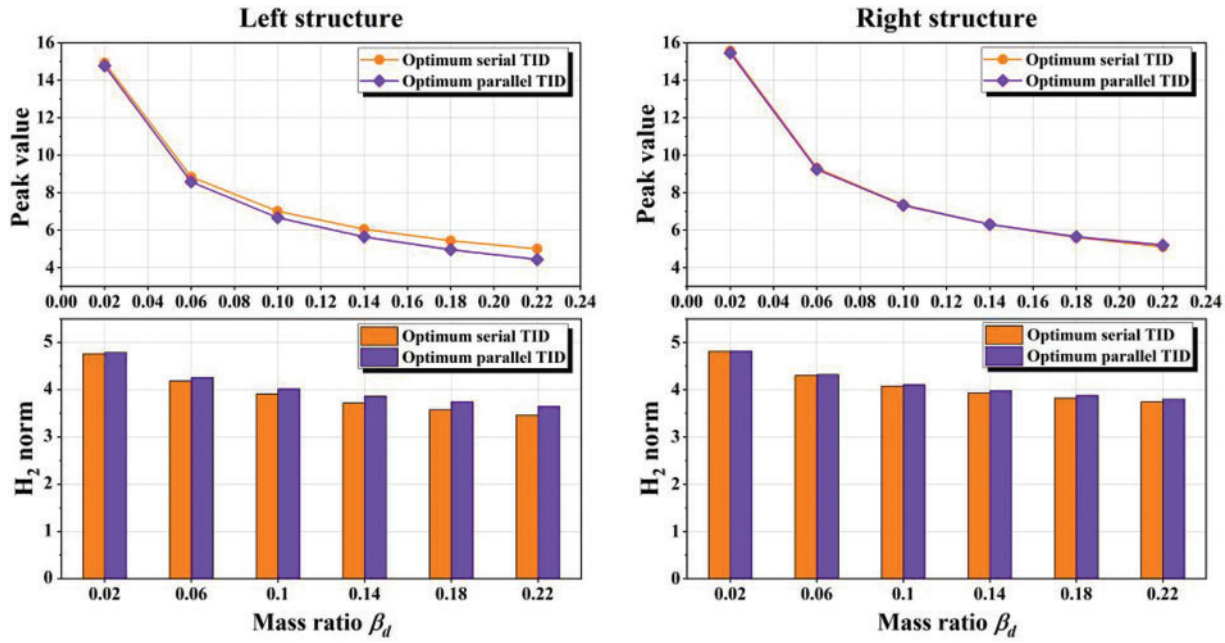

Figure 19: Considering the different values of mass ratio β_d, the related calculation results of normalized displacement graphs of left structure and right structure under the coupling of serial TID and parallel TID (In the figure, the line graph represents the maximum value of the normalized displacement, and the column graph represents the area S enclosed by the displacement curve and the coordinate axis, that is, the H_2 norm)

The above analysis results show that when the mass of the damper is small compared with that of the left structure ($\beta_d \leq 0.1$), increasing the mass of the damper can really enhance the damping effect. However, when the mass of the damper increases gradually compared with that of the left structure ($\beta_d > 0.1$), the constraints of actual cost and site conditions should be considered, and the damping effect of the damper with large mass compared with the left structure is not obviously improved. In addition, when controlling the peak displacement of adjacent buildings under earthquake, parallel TID should be given priority. If H_2 norm is taken into account, it is better to choose serial TID.

5.3 Robustness Performance Analysis

Optimization parameters in practical engineering often change. In order to make adjacent buildings achieve more robust vibration control effect, it is necessary to analyze their robustness. Fig. 20 is the robustness analysis curve of the left structure and the right structure under the coupling of serial TID and parallel TID. The optimum frequency ratio f_{dopt} and the optimum damping ratio ξ_{dopt} are the influencing factors.

As shown in Fig. 20, slightly change the damping ratio the value of ξ_{dopt} has little influence on the vibration control effect of adjacent buildings under serial and parallel TID coupling, and only causes slight changes at the peak position, which indicates that the normalized displacement is not sensitive to the change of damping ratio. However, if the frequency ratio f_{dopt} is slightly changed, it can be seen from Fig. 20 that the normalized displacement change is significant. In addition, it can be seen from

the Fig. 20d that there is a special case, that is, when the frequency ratio f_{dopt} of the right structure under parallel TID coupling decreases, the amplitude of change is so large that the change of wave peak height cannot be accurately seen.

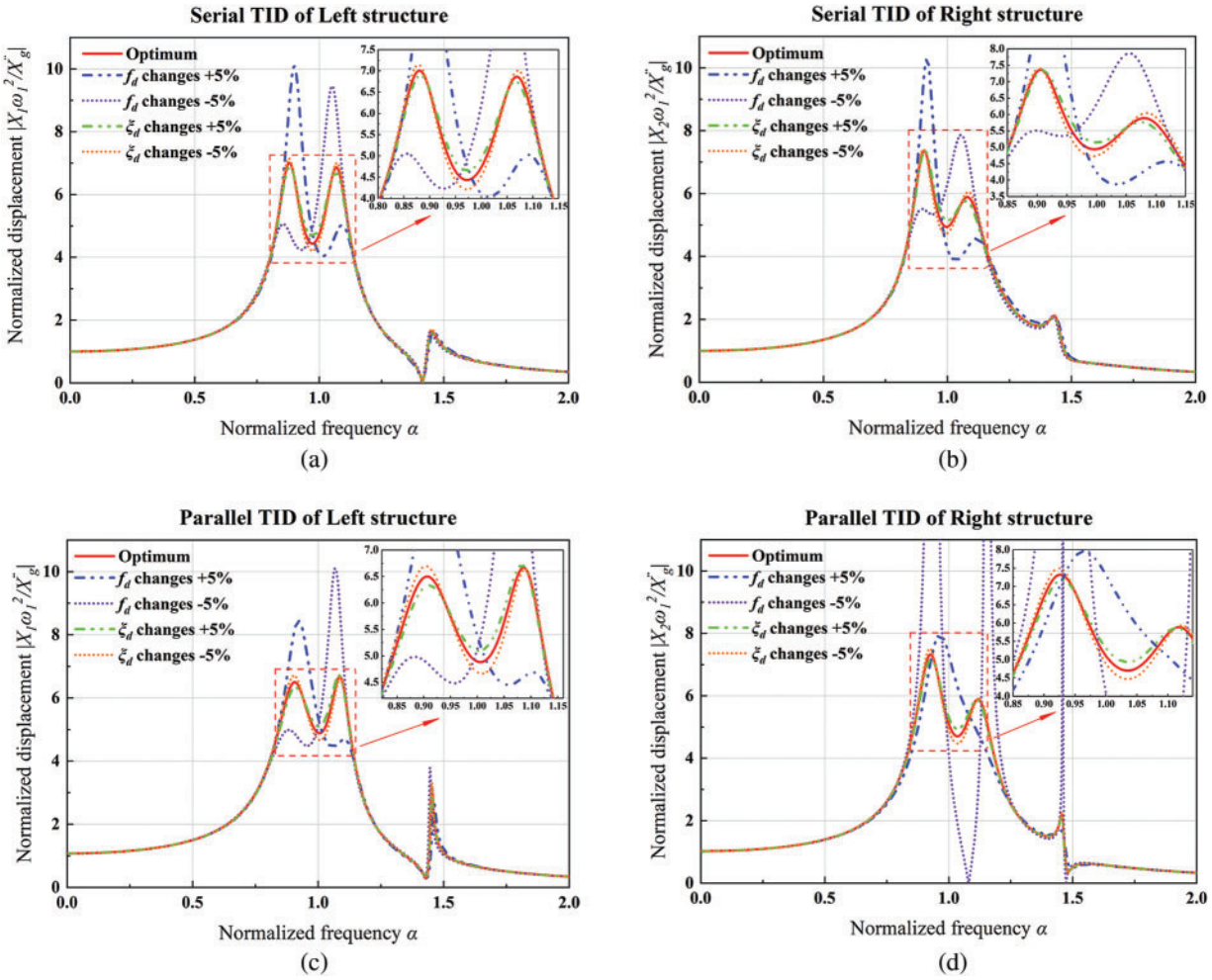

Figure 20: Robustness performance analysis curves of left structure and right structure of adjacent buildings under the coupling of serial TID and parallel TID: (a) Serial TID is coupled with the left structure; (b) Serial TID is coupled with the right structure; (c) Parallel TID is coupled with the left structure; (d) Parallel TID is coupled with the right structure ($\beta_2 = 1.0$, $\beta_d = 0.1$, $\lambda_2 = 1.0$, $\lambda_s = 0.5$)

To further determine the size of the change, the detailed drawing of Fig. 20d is shown in Fig. 21. It can be seen from the figure that the right structure in adjacent buildings under the coupling of parallel TIDs is extremely sensitive to the reduction of frequency ratio f_{dopt}, and the displacement after the change is very large, and the vibration control effect decreases obviously. The above results show that, in the actual engineering structure design, in order to achieve more robust vibration control effect of adjacent building structures, the change of stiffness is more worthy of attention than the change of damping of TID.

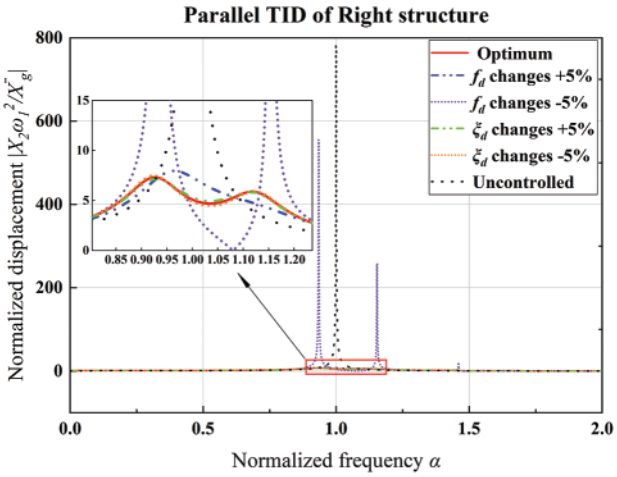

Figure 21: Robust performance analysis curve of the right structure of adjacent buildings under the coupling of parallel TID

6 Time Domain Simulation

6.1 Vibration Control Performance

In the foregoing analysis, we assume that the external excitation is white noise excitation with evenly distributed energy at all frequencies, but the ground motion caused by earthquake is actually not ideal white noise [35]. Therefore, it is necessary to simulate and verify the seismic performance of adjacent buildings under the coupling of serial TID and parallel TID. Taking two ten-story frame structures as an example, the relevant parameters of the adjacent building structures are: $m_1 = m_2 = 5.897 \times 10^4\ kg$, $c_1 = c_2 = 67.4 \times 10^3\ N \cdot s/m$, $c_s = 33.7 \times 10^3\ N \cdot s/m$, $k_1 = k_2 = 4.81 \times 10^7\ N/m$, $k_s = 2.405 \times 10^7\ N/m$ [50], $\beta_d = 0.1$, $\beta_t = 0.1$ and relevant parameters of dampers are determined in Table 4. The external excitation is four commonly used seismic waves, namely: El Centro (May 18, 1940), Taft (July 21, 1952), Loma Prieta (October 17, 1989) and Chi-Chi (September 21, 1999) [2,35]. Fig. 22 shows the acceleration time history of four types of seismic waves. Under the excitation of four types of seismic waves, the displacement time history curves of adjacent buildings coupled with different dampers are shown in Figs. 23 and 24.

Table 4: Relevant parameters of damper

Damper types	Structure types	Optimum solutions	
		Optimum frequency ratio f_{dopt}	Optimum damping ratio ξ_{dopt}
Serial TID	Left structure	0.964	0.111
	Right structure	1.006	0.134
Parallel TID	Left structure	1.017	0.121
	Right structure	1.078	0.120
Classic TMD	Left structure	0.938	0.115
	Right structure	0.982	0.126

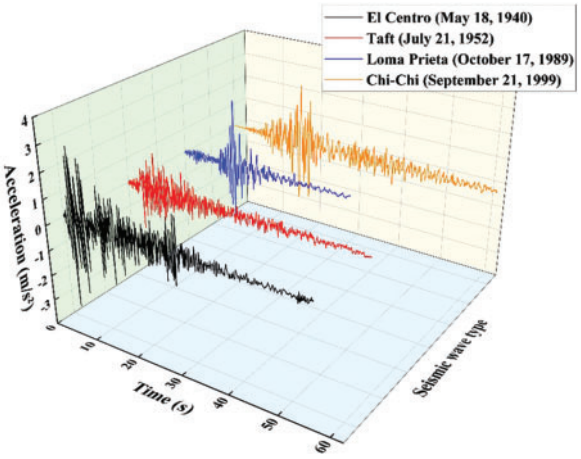

Figure 22: Acceleration time history curves of four types of seismic waves

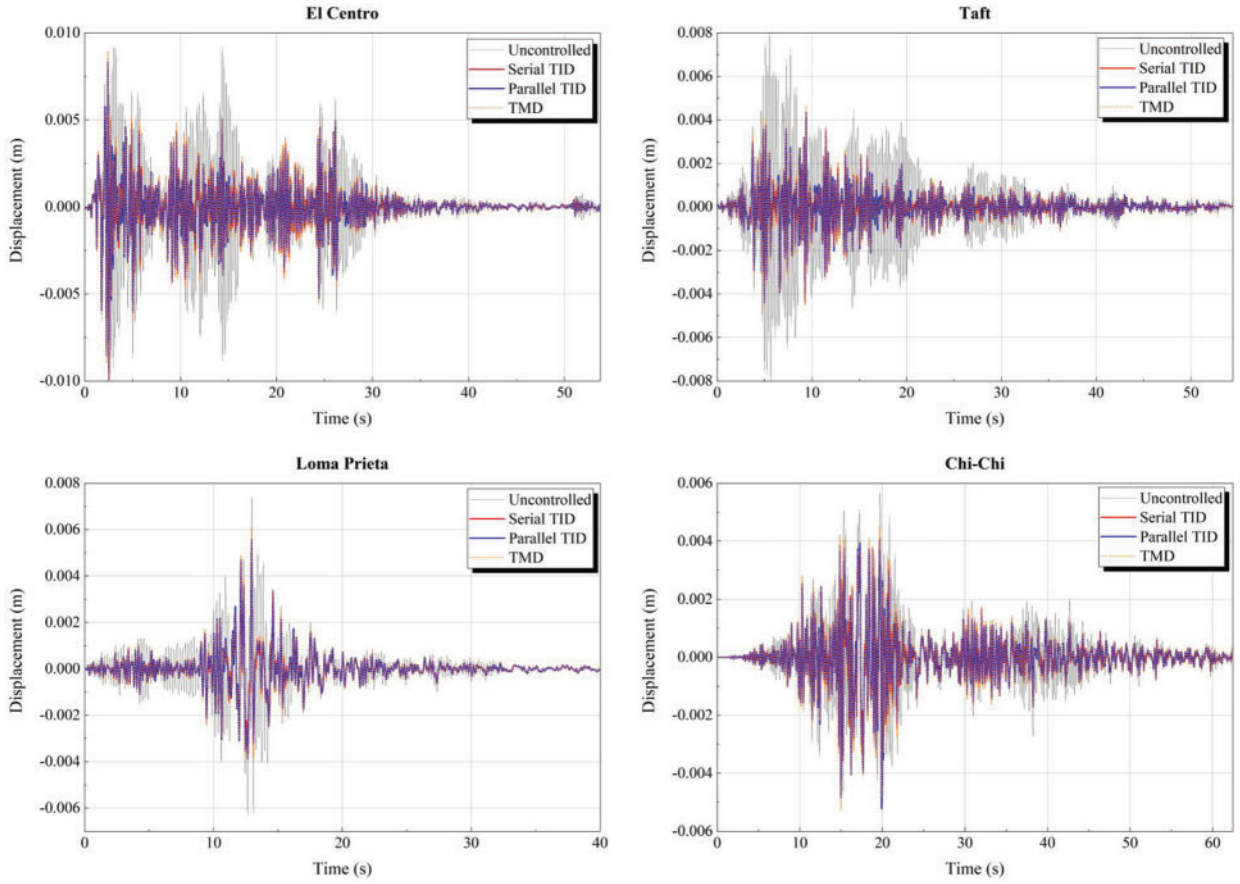

Figure 23: Displacement time history graphs of the left structure under four types of seismic waves excitation

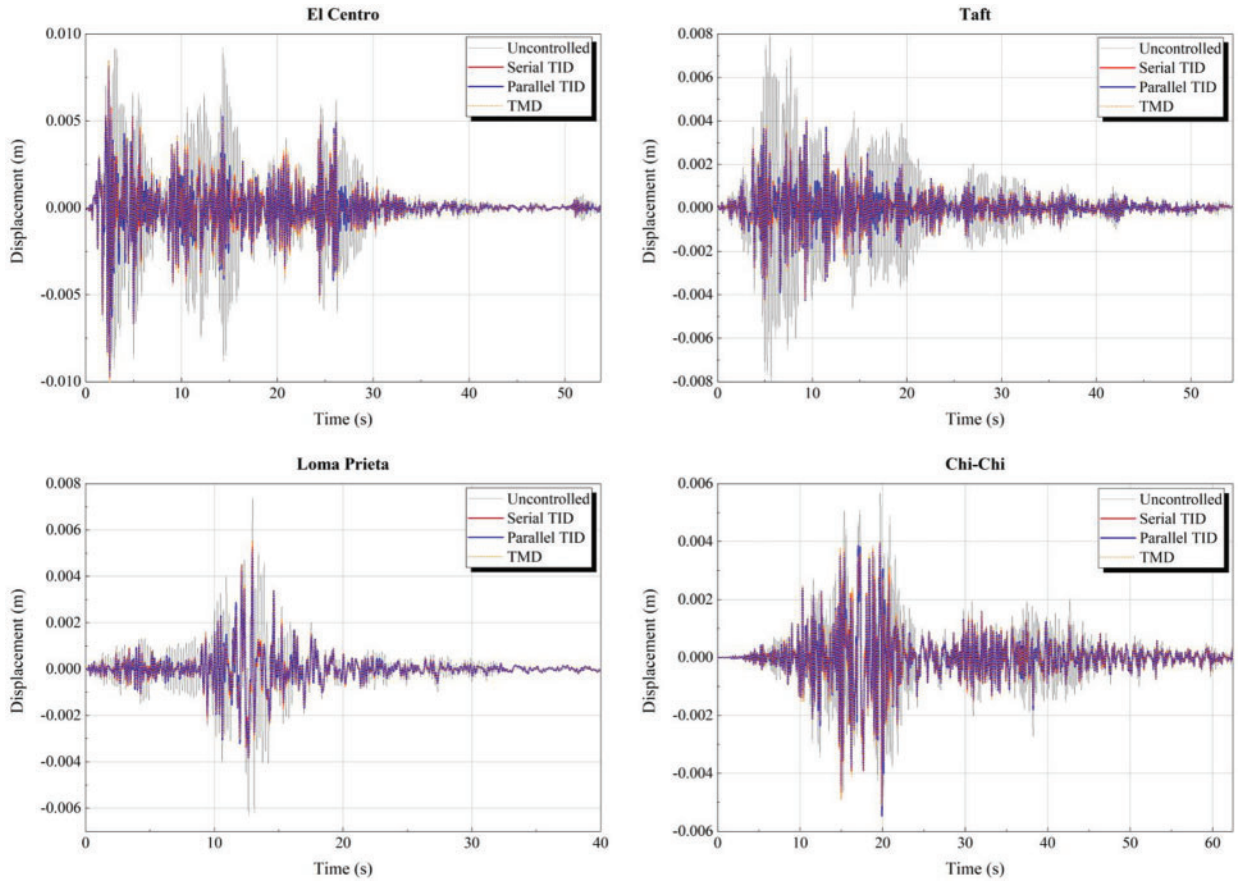

Figure 24: Displacement time history graphs of the right structure under four types of seismic waves excitation

It can be seen from Fig. 23 that under the excitation of different types of seismic waves, compared with the displacement of the left structure in the uncontrolled state, the three dampers have good damping effects in the whole range. Comparing the displacement of three dampers, it is found that the displacement of classical TMD is slightly larger than that of serial or parallel TID. In order to make a more accurate comparison, the peak and root mean square values of the displacement of the left structure coupled with three different types of dampers are summarized, as shown in Table 5. It can be seen from Table 5 that, compared with the peak displacement in uncontrolled state, the peak control effect of the serial TID is at least 10.1% and at most 47.8%; the peak control effect of parallel TID is at least 9.5% and at most 45.9%; the peak control effect of classic TMD is at least 2.8% and at most 42.3%. As for the control effect of RMS, the control effect of serial TID is at least 21.6% and at most 53.2%; the control effect of parallel TID is at least 18.6% and at most 51.3%, the control effect of classical TMD is at least 14.7% and at most 49.4%. It can be found that under the vibration control of the above model, the root mean square control effect is often greater than the peak damping ratio. The above results show that for the left structure coupled with three types of dampers, all of them can achieve good damping effect, among which the serial TID has the best damping effect, the parallel TID is the second, and the classic TMD is the last.

Table 5: Peak values and root mean square values of displacement time history under different seismic waves excitation

Seismic wave types	Structure types	Peak (*mm*)				RMS (*mm*)			
		UC	Serial TID	Parallel TID	TMD	UC	Serial TID	Parallel TID	TMD
El Centro	LS	9.22	8.29	8.34	8.96	2.14	1.32	1.33	1.42
	RS	9.22	8.06	8.17	8.49	2.14	1.31	1.32	1.35
Taft	LS	8.06	4.21	4.36	4.65	1.58	0.74	0.77	0.80
	RS	8.06	3.94	3.97	4.19	1.58	0.76	0.78	0.77
Loma Prieta	LS	7.41	5.45	5.58	6.11	1.02	0.67	0.71	0.73
	RS	7.41	5.27	5.19	5.55	1.02	0.67	0.68	0.69
Chi-Chi	LS	5.68	3.87	4.08	4.53	1.02	0.80	0.83	0.87
	RS	5.68	3.89	3.94	4.03	1.02	0.79	0.80	0.81

Note: In the table, (1) "LS" means the left structure; (2) "RS" means the right structure; (3) "UC" means the uncontrolled state of adjacent buildings.

It can be seen from Fig. 24 that, similar to the left structure, under the excitation of different types of seismic waves, compared with the displacement of the right structure in the uncontrolled state, the three dampers have good damping effects in the whole range. Comparing the displacement of three dampers, it is found that the displacement of classic TMD is slightly larger than that of serial or parallel TID. It can be seen from Table 5 that, for the right structure, compared with the peak displacement in uncontrolled state, the peak control effect of the serial TID is at least 12.6% and at most 51.1%; the peak control effect of parallel TID is at least 11.4% and at most 50.7%; the peak control effect of classic TMD is at least 7.9% and at most 48.0%. As for the control effect of RMS, the control effect of serial TID is at least 22.6% and at most 51.9%; the control effect of parallel TID is at least 21.6% and at most 50.6%, the control effect of classical TMD is at least 20.6% and at most 51.3%. The above results show that for the right structure coupled with three types of dampers, all of them can achieve good damping effect, among which the serial TID has the best damping effect, the parallel TID is the second, and the classic TMD is the last. In addition, it can be found that the right structure can achieve better damping effect than the left structure when the adjacent buildings are coupled with the same damper.

6.2 Energy Collection

As mentioned in Section 2.2, installing the roller generator inside the inerter device can collect part of the vibration energy during the earthquake and make use of it. Therefore, in this paper, we connect the left structure with the TID to collect the vibration energy of the building structure. Based on the fact that the power consumption of the external resistor is basically equivalent to that of the TID buffer element, the power calculation formula can be expressed as $P = c_1\dot{x}_1^2$. Fig. 25 shows the energy collection graph of the left structure under the excitation of four types of seismic waves, coupled with serial TID and parallel TID. It can be seen from Fig. 25 that the energy power value of the left structure under the excitation of El Centro seismic waves is larger than that of the other three types of seismic waves, showing the best energy collection effect, and the energy collection effects of the other three types of seismic waves are similar. For more accurate comparison, the peak and average values

of power in Fig. 25 are summarized in Table 6. As can be seen from Table 6, under the excitation of the same type of seismic wave, in most cases, the peak value and average value of the collected power of the left structure with parallel TID coupling are higher than those of the left structure with serial TID, this shows that, on the premise of similar vibration control effect, the parallel TID should be preferred for the energy collection of the left structure of adjacent buildings.

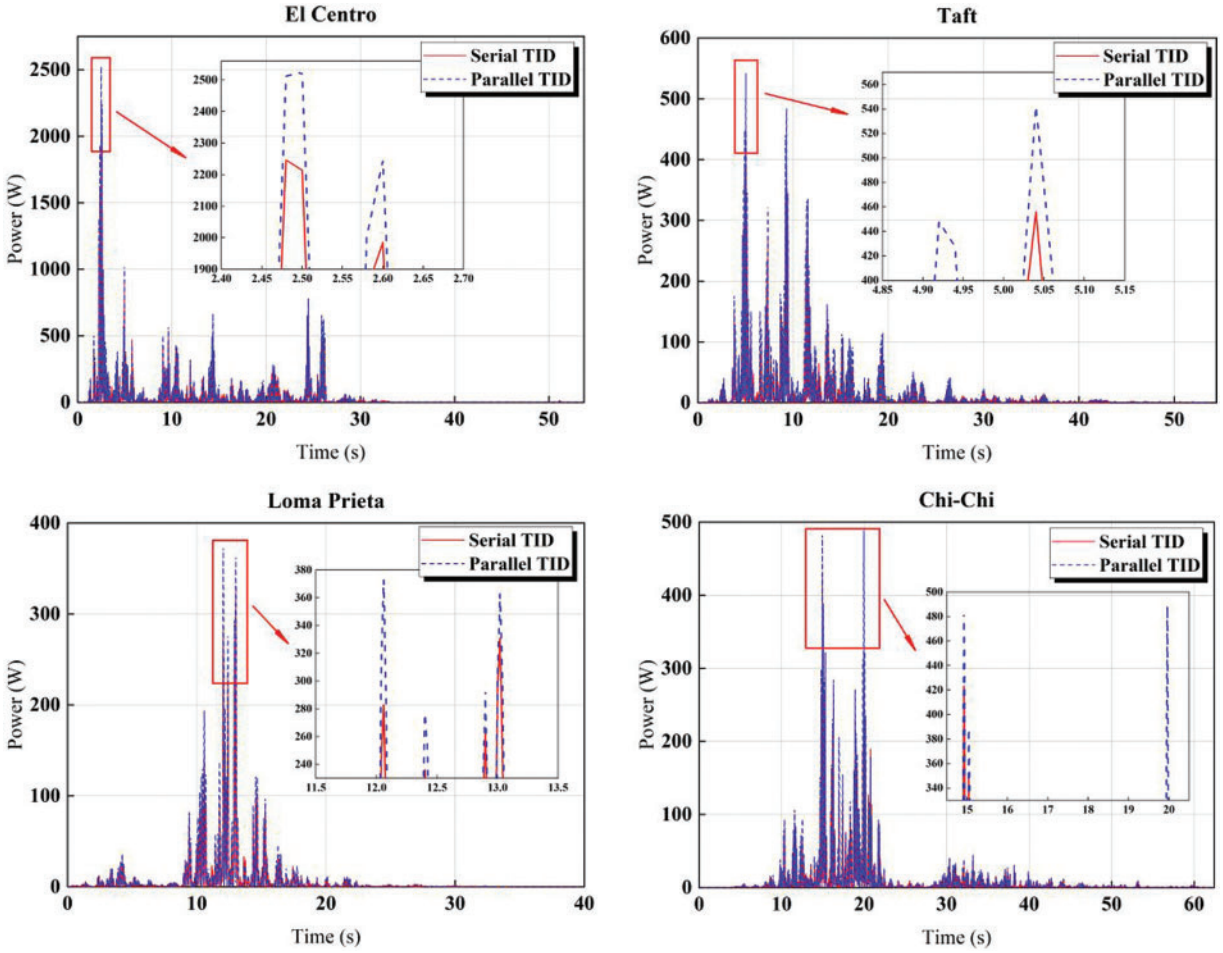

Figure 25: Energy collection graphs of the left structure under four types of seismic waves excitation

Table 6: Energy collection under different seismic waves excitation

Seismic wave types	Peak (W)		Average (W)	
	Serial TID	Parallel TID	Serial TID	Parallel TID
El Centro	2246.25	2525.56	38.47	44.66
Taft	455.94	542.11	15.15	12.42
Loma Prieta	330.81	373.09	6.45	7.79
Chi-Chi	423.10	488.76	9.23	10.85

It can be seen from Table 6 that the left structure under the excitation of El Centro seismic wave has a remarkable energy collection effect, with its power peak value reaching 2525.56 W and power root mean square value reaching 44.66 W. According to the calculation, the energy collected in the whole period of El Centro seismic wave is 1.44×10^5 J. Compared with the classical TMD, it is known from the analysis results in Section 5.2 that the vibration reduction effect of TID is better than that of the classic TMD. At the same time, TID has the advantage of collecting energy, when an earthquake occurs, it can store part of the energy for the structure itself, and use it according to the actual situation. Therefore, in real life, when the economic cost is similar, compared with the classic TMD, TID should be preferred to achieve the dual effects of structural vibration control and energy collection.

7 Conclusions

In this paper, two types of tuned inerter damper (TID) adjacent building damping systems composed of springs, inerters and dampers in serial or in parallel were proposed. H_2 norm criterion was adopted to optimize and adjust the damping system of adjacent buildings, so that the system had the best damping performance under the random excitation of white noise. The parameter analysis, frequency response analysis, robustness analysis, time history response analysis and energy collection analysis of the system were carried out successively. Through the above analysis, the following conclusions are drawn:

(1) As for the H_2 norm optimization results of adjacent buildings, when considering the value of mass ratios β_2 and β_d, only the change trend of f_{dopt} and ξ_{dopt} of the right structure under the coupling of serial TID was fluctuating, and the rest changed smoothly. When considering the values of stiffness ratio λ_2 and λ_s, the change trend of f_{dopt} and ξ_{dopt} of the right structure under the coupling of serial TID and parallel TID were fluctuating, while the rest changed smoothly. For the left structure, the ξ_{dopt} of serial TID and the f_{dopt} of parallel TID were fluctuating, and the rest of the situation changed smoothly.

(2) When studying the displacement frequency response of adjacent buildings, it was found that when $\beta_d = 0.1$, based on the peak displacement, compared with the classic TMD, the parallel TID had a better damping effect on the left structure, but the improvement effect of TID on the right structure was not obvious. Based on the H_2 norm in the normalized frequency range of 0∼2.0, compared with the classic TMD, the serial TID had a better control effect on the left structure, but the improvement effect of TID on the right structure was not obvious. Changing the mass ratio, when $\beta_d \leq 0.1$, increasing the damper mass could obviously enhance the damping effect, but when $\beta_d > 0.1$, the enhancement effect was not obvious. In addition, parallel TID had obvious advantages in controlling the peak displacement of the left structure, and the larger β_d is, the more obvious it is, but it had no obvious superiority for the right structure. Serial TID had obvious advantages in controlling H_2 norm of the left structure and the right structure, and the larger β_d is, the more obvious it is.

(3) As for the seismic robustness of adjacent building structures under TID coupling, the normalized displacement was less affected by the optimum damping ratio ξ_{dopt}, but significantly affected by the optimum frequency ratio f_{dopt}, especially for the right structure under parallel TID coupling. In actual engineering, when facing the vibration problem of adjacent buildings under white noise excitation, if we want to achieve more robust control, the first thing we need to pay attention to was the stiffness of the damper, followed by the damping.

(4) The time history analysis results of adjacent buildings excited by four types of seismic waves showed that all three types of dampers could achieve a good damping effect, among which the serial TID was the best, the parallel TID was the second, and the classic TMD was the last. In addition, for adjacent buildings coupled with the same damper, the right structure could often achieve a better

damping effect than the left structure. According to the time history analysis of energy collection of adjacent buildings excited by four types of seismic waves, it was found that the left structure excited by El Centro seismic waves had the best energy collection effect, with its instantaneous peak power reaching 2525.56 W and the root mean square power reaching 44.66 W in the whole period. According to the calculation, the energy collected in the whole period of El Centro seismic wave was 1.44×10^5 J. In addition, when collecting the vibration energy of adjacent building structures under earthquake excitation, it was found that parallel TID should be given priority.

Based on the above analysis results, in general, the proposed TIDs with different connection modes had significant effects on the vibration control of adjacent buildings, and their performance was superior to that of classic TMDs. In addition, this type of TID also had the function of energy collection, which further expands its application range. The research results of this article could provide some reference significance for the vibration control research of adjacent buildings, however, the application of TIDs proposed in this paper in practical engineering needs further research and demonstration to achieve better vibration control effects.

Acknowledgement: The authors are very grateful to the editors and all anonymous reviewers for their insightful comments.

Funding Statement: This research was funded by the Natural Science Research Project of Higher Education Institutions in Anhui Province (Grant No. 2022AH040045), the Anhui Provincial Natural Science Foundation (Grant No. 2008085QE245), the Project of Science and Technology Plan of Department of Housing and Urban-Rural Development of Anhui Province (Grant No. 2021-YF22).

Author Contributions: The authors confirm contribution to the paper as follows: study conception and design: Xiaofang Kang and Jian Wu; data collection: Jian Wu and Xinqi Wang; analysis and interpretation of results: Jian Wu and Shancheng Lei; draft manuscript preparation: Xiaofang Kang and Jian Wu. All authors reviewed the results and approved the final version of the manuscript.

Availability of Data and Materials: No new data and materials were created or analyzed in this study. Data and material sharing are not applicable for this article.

Conflicts of Interest: The authors declare that they have no conflicts of interest to report regarding the present study.

References

1. Lee, C. H., Chen, Y. C., Wang, F. C. (2015). Earthquake suppression for a scale building model employing inclined inerter. *IEEE/SICE International Symposium on System Integration (SII)*, pp. 828–833. Nagoya, Japan.
2. Luo, Y. (2017). *Study on parameter optimization of structure vibration control with electromagnetic energy collecting tuned mass damper*. Hunan University of Science and Technology, China.
3. Housner, G. W., Bergman, L. A., Caughey, T. K., Chassiakos, A. G., Claus, R. O. et al. (1997). Structural control: Past, present, and future. *Journal of Engineering Mechanics, 123,* 897–971.
4. Soong, T., Spencer, B. F. (2002). Supplemental energy dissipation: State-of-the-art and state-of-the-practice. *Engineering Structures, 24(3),* 243–259.
5. Frahm, H. (1911). *Device for damping vibrations of bodies*. US989958, USA.
6. Kareem, A., Kijewski, T., Tamura, Y. (1999). Mitigation of motions of tall buildings with specific examples of recent applications. *Wind and Structures, 2(3),* 201–251.

7. Zuo, H., Bi, K., Hao, H., Ma, R. (2021). Influences of ground motion parameters and structural damping on the optimum design of inerter-based tuned mass dampers. *Engineering Structures, 227,* 111422.
8. Zhu, H., Li, Y., Shen, W., Zhu, S. (2019). Mechanical and energy-harvesting model for electromagnetic inertial mass dampers. *Mechanical Systems and Signal Processing, 120,* 203–220.
9. Nakamura, Y., Fukukita, A., Tamura, K., Yamazaki, I., Matsuoka, T. et al. (2014). Seismic response control using electromagnetic inertial mass dampers. *Earthquake Engineering & Structural Dynamics, 43,* 507–527.
10. Ma, R., Bi, K., Hao, H. (2019). A novel rotational inertia damper for heave motion suppression of semisubmersible platform in the shallow sea. *Structural Control & Health Monitoring, 26(7),* e2368.
11. Ma, R., Bi, K., Hao, H. (2020). Using inerter-based control device to mitigate heave and pitch motions of semi-submersible platform in the shallow sea. *Engineering Structures, 207,* 110248.
12. Garrido, H., Curadelli, O., Ambrosini, D. (2013). Improvement of tuned mass damper by using rotational inertia through tuned viscous mass damper. *Engineering Structures, 56,* 2149–2153.
13. Javidialesaadi, A., Wierschem, N. E. (2018). Optimal design of rotational inertial double tuned mass dampers under random excitation. *Engineering Structures, 165,* 412–421.
14. Li, Y., Li, S., Chen, Z. (2020). Optimization and wind-induced vibration suppression of rotational inertia double tuned mass damper. *Journal of Vibration Engineering, 33(2),* 295–303.
15. Marian, L., Giaralis, A. (2014). Optimal design of a novel tuned mass-damper-inerter (TMDI) passive vibration control configuration for stochastically support-excited structural systems. *Probabilistic Engineering Mechanics, 38,* 156–164.
16. Cao, L., Li, C. (2019). Tuned tandem mass dampers-inerters with broadband high effectiveness for structures under white noise base excitations. *Structural Control & Health Monitoring, 26(4),* e2319.
17. Zhao, X., Li, C., Cao, L. (2022). Control performance of structure-NFVD-TTMDI. *Journal of Vibration Engineering, 35(1),* 55–63.
18. Zhao, Z., Zhang, R., Jiang, Y., Pan, C. (2019). A tuned liquid inerter system for vibration control. *International Journal of Mechanical Sciences, 164,* 105171.
19. Lazar, I., Neild, S., Wagg, D. (2014). Using an inerter-based device for structural vibration suppression. *Earthquake Engineering & Structural Dynamics, 43(8),* 1129–1147.
20. Lazar, I., Neild, S., Wagg, D. (2016). Vibration suppression of cables using tuned inerter dampers. *Engineering Structures, 122,* 62–71.
21. Sun, L., Hong, D., Chen, L. (2017). Cables interconnected with tuned inerter damper for vibration mitigation. *Engineering Structures, 151,* 57–67.
22. Deastra, P., Wagg, D., Sims, N., Akbar, M. (2020). Tuned inerter dampers with linear hysteretic damping. *Earthquake Engineering & Structural Dynamics, 49(12),* 1216–1235.
23. Shi, B., Yang, J., Jiang, J. Z. (2022). Tuning methods for tuned inerter dampers coupled to nonlinear primary systems. *Nonlinear Dynamics, 107,* 1663–1685.
24. Bin, T., Wang, X., Fang, H., Wang, W. (2020). Analysis of mitigating performance of tuned inerter mass dampers. *Noise and Vibration Control, 40(4),* 223–226.
25. De Domenico, D., Ricciardi, G., Zhang, R. (2020). Optimal design and seismic performance of tuned fluid inerter applied to structures with friction pendulum isolators. *Soil Dynamics and Earthquake Engineering, 132,* 106099.
26. de Domenico, D., Deastra, P., Ricciardi, G., Sims, N. D., Wagg, D. J. (2019). Novel fluid inerter based tuned mass dampers for optimised structural control of base-isolated buildings. *Journal of the Franklin Institute-Engineering and Applied Mathematics, 356(14),* 7626–7649.
27. Liang, Q., Li, L. (2020). Optimal design for a novel inerter-based clutching tuned mass damper system. *Journal of Vibration and Control, 26(21–22),* 2050–2059.
28. Smith, M. C. (2002). Synthesis of mechanical networks: The inerter. *IEEE Transactions on Automatic Control, 47,* 1648–1662.

29. Hwang, J. S., Kim, J., Kim, Y. M. (2007). Rotational inertia dampers with toggle bracing for vibration control of a building structure. *Engineering Structures, 29(6),* 1201–1208.
30. Swift, S. J., Smith, M. C., Glover, A. R., Papageorgiou, C., Gartner, B. et al. (2013). Design and modelling of a fluid inerter. *International Journal of Control, 86(11),* 2035–2051.
31. De Domenico, D., Ricciardi, G. (2018). An enhanced base isolation system equipped with optimal tuned mass damper inerter (TMDI). *Earthquake Engineering & Structural Dynamics, 47(5),* 1169–1192.
32. Javidialesaadi, A., Wierschem, N. E. (2018). Three-element vibration absorber-inerter for passive control of single-degree-of-freedom structures. *Journal of Vibration and Acoustics-Transactions of the ASME, 140(6),* 061007.
33. Chen, M. Z. Q., Papageorgiou, C., Scheibe, F., Wang, F. C., Smith, M. C. (2009). The missing mechanical circuit element. *IEEE Circuits and Systems Magazine, 9,* 10–26.
34. Papageorgiou, C., Houghton, N. E., Smith, M. C. (2009). Experimental testing and analysis of inerter devices. *Journal of Dynamic Systems Measurement and Control-Transactions of the ASME, 131,* 011001.
35. Qian, F., Luo, Y., Sun, H., Tai, W., Zuo, L. (2019). Optimal tuned inerter dampers for performance enhancement of vibration isolation. *Engineering Structures, 198,* 109464.
36. Ikago, K., Saito, K., Inoue, N. (2012). Seismic control of single-degree-of-freedom structure using tuned viscous mass damper. *Earthquake Engineering & Structural Dynamics, 41(3),* 453–474.
37. Dai, J., Xu, Z., Gai, P., Hu, Z. (2021). Optimal design of tuned mass damper inerter with a Maxwell element for mitigating the vortex-induced vibration in bridges. *Mechanical Systems and Signal Processing, 148,* 107180.
38. Dai, J., Xu, Z., Gai, P. (2019). Tuned mass-damper-inerter control of wind-induced vibration of flexible structures based on inerter location. *Engineering Structures, 199,* 109585.
39. Sun, H., Zuo, L., Wang, X., Peng, J., Wang, W. (2019). Exact H_2 optimal solutions to inerter-based isolation systems for building structures. *Structural Control & Health Monitoring, 26(6),* e2357.
40. Jangid, R. S. (2021). Optimum tuned inerter damper for base-isolated structures. *Journal of Vibration Engineering & Technologies, 9,* 1483–1497.
41. Gonzalez-Buelga, A., Clare, L. R., Neild, S. A., Jiang, J. Z., Inman, D. J. (2015). An electromagnetic inerter-based vibration suppression device. *Smart Materials and Structures, 24,* 055015.
42. Shen, W., Niyitangamahoro, A., Feng, Z., Zhu, H. (2019). Tuned inerter dampers for civil structures subjected to earthquake ground motions: Optimum design and seismic performance. *Engineering Structures, 198,* 109470.
43. Crandall, S. H., Mark, W. D. (1963). *Random vibration in mechanical systems*. USA: Academic Press.
44. Asami, T., Nishihara, O., Baz, A. M. (2002). Analytical solutions to H∞ and H_2 optimization of dynamic vibration absorbers attached to damped linear systems. *Journal of Vibration and Acoustics-Transactions of the ASME, 124(2),* 284–295.
45. Palacios-Quiñonero, F., Rubió-Massegú, J., Rossell, J. M., Karimi, H. R. (2019). Design of inerter-based multi-actuator systems for vibration control of adjacent structures. *Journal of the Franklin Institute, 356(14),* 7785–7809.
46. Djerouni, S., Elias, S., Abdeddaim, M., Rupakhety, R. (2022). Optimal design and performance assessment of multiple tuned mass damper inerters to mitigate seismic pounding of adjacent buildings. *Journal of Building Engineering, 48,* 103994.
47. Luo, Y., Sun, H., Wang, X. (2019). The H_2 parametric optimization and structural vibration suppression of electromagnetic tuned mass-inerter dampers. *Engineering Mechanics, 36(4),* 89–99.
48. Sun, H., Luo, Y., Wang, X., Yu, J., Peng, J. (2018). Parametric optimization and vibration control of electromagnetic tuned mass-inerter dampers for the structures. *Journal of Shenyang Jianzhu University (Natural Science), 34(3),* 410–418.

49. Rana, R., Soong, T. T. (1998). Parametric study and simplified design of tuned mass dampers. *Engineering Structures, 20(3),* 193–204.
50. Luo, Y., Sun, H., Wang, X. (2018). H_2 parameters optimization and vibration reduction analysis of electromagnetic tuned mass damper. *Journal of Vibration Engineering, 31(3),* 529–538.

Appendix A. The numerator and denominator coefficients of Eq. (7) are as follows:

$$\begin{cases} B_0^s = \lambda_d(\lambda_2 + (\beta_2+1)\lambda_s) \\ B_1^s = 2(\beta_d f_d \xi_d(\lambda_2 + (\beta_2+1)\lambda_s) + \xi_1\lambda_d(\mu_2 + (\beta_2+1)\mu_s)) \\ B_2^s = \beta_2\lambda_d + \beta_d(4\xi_1 f_d\xi_d(\mu_2 + (\beta_2+1)\mu_s) + \lambda_2 + (\beta_2+1)\lambda_s) \\ B_3^s = 2\beta_d(\beta_2 f_d\xi_d + \mu_2\xi_1 + (\beta_2+1)\xi_1\mu_s) \\ B_4^s = \beta_2\beta_d \end{cases} \tag{A1}$$

$$\begin{cases} A_0^s = \lambda_d(\lambda_s + \lambda_2(\lambda_s+1)) \\ A_1^s = 2(\lambda_2(\beta_d f_d\xi_d(\lambda_s+1) + \xi_1\lambda_d(\mu_s+1)) + \beta_d f_d\xi_d\lambda_s + \xi_1\lambda_d(\mu_2 + (\mu_2+1)\lambda_s + \mu_s)) \\ A_2^s = \beta_d(\lambda_s(4(\mu_2+1)\xi_1 f_d\xi_d + \lambda_d + 1) + \lambda_2(4\xi_1 f_d\xi_d + 4\xi_1 f_d\xi_d\mu_s + \lambda_d + \lambda_s + 1) + 4\xi_1 f_d\xi_d(\mu_2+\mu_s)) \\ \quad + \lambda_d\left(\lambda_2 + 4\mu_2\xi_1^2 + \beta_2(\lambda_s+1) + \lambda_s + 4\mu_2\xi_1^2\mu_s + 4\xi_1^2\mu_s\right) \\ A_3^s = 2(\beta_d(\beta_2 f_d\xi_d + 4\mu_2\xi_1^2 f_d\xi_d + \lambda_s((\beta_2+1)f_d\xi_d + (\mu_2+1)\xi_1) + \lambda_2(f_d\xi_d + \xi_1(\mu_s+1)) + 4\xi_1^2 f_d\xi_d\mu_s \\ \quad + 4\mu_2\xi_1^2 f_d\xi_d\mu_s + \mu_2\xi_1\lambda_d + \xi_1\lambda_d\mu_s + \mu_2\xi_1 + \xi_1\mu_s) + \beta_d^2 f_d\xi_d(\lambda_2+\lambda_s) + \xi_1\lambda_d(\mu_2 + \beta_2(\mu_s+1) + \mu_s)) \\ A_4^s = \beta_2(\beta_d(4\xi_1 f_d\xi_d + 4\xi_1 f_d\xi_d\mu_s + \lambda_d + \lambda_s + 1) + \lambda_d) + \beta_d(4\xi_1(\mu_s((\beta_d+1)f_d\xi_d + \xi_1) + \mu_2((\beta_d+1)f_d\xi_d \\ \quad + \xi_1(\mu_s+1))) + \lambda_2 + \lambda_s) \\ A_5^s = 2\beta_d(\beta_2((\beta_d+1)f_d\xi_d + \xi_1(\mu_s+1)) + \xi_1(\mu_2+\mu_s)) \\ A_6^s = \beta_2\beta_d \end{cases} \tag{A2}$$

Appendix B. The numerator coefficient of Eq. (8) is as follows:

$$\begin{cases} C_0^s = \lambda_d(\beta_2(\lambda_s+1) + \lambda_s) \\ C_1^s = 2(\beta_2(\beta_d f_d\xi_d(\lambda_s+1) + \xi_1\lambda_d(\mu_s+1)) + \beta_d f_d\xi_d\lambda_s + \xi_1\lambda_d\mu_s) \\ C_2^s = \beta_d(4\xi_1 f_d\xi_d\mu_s + \lambda_s) + \beta_2(\beta_d(4\xi_1 f_d\xi_d + 4\xi_1 f_d\xi_d\mu_s + \lambda_d + \lambda_s + 1) + \lambda_d) \\ C_3^s = 2\beta_d(\beta_2((\beta_d+1)f_d\xi_d + \xi_1(\mu_s+1)) + \xi_1\mu_s) \\ C_4^s = \beta_2\beta_d \end{cases} \tag{B1}$$

Appendix C. The numerator and denominator coefficients of Eq. (9) are as follows:

$$\begin{cases} B_0^p = \lambda_d(\lambda_2(\beta_d+1)+(\beta_2+\beta_d+1)\lambda_s) \\ B_1^p = 2(\beta_d f_d\xi_d(\lambda_2+(\beta_2+1)\lambda_s)+\xi_1\lambda_d(\mu_2(\beta_d+1)+(\beta_2+\beta_d+1)\mu_s)) \\ B_2^p = \beta_2\lambda_d+\beta_d(4\mu_2\xi_1 f_d\xi_d+\beta_2(4\xi_1 f_d\xi_d\mu_s+\lambda_d+\lambda_s)+4\xi_1 f_d\xi_d\mu_s+\lambda_2+\lambda_s) \\ B_3^p = 2\beta_d(\beta_2 f_d\xi_d+\mu_2\xi_1+(\beta_2+1)\xi_1\mu_s) \\ B_4^p = \beta_2\beta_d \end{cases} \tag{C1}$$

$$\begin{cases} A_0^p = \lambda_d(\lambda_s+\lambda_2(\lambda_s+1)) \\ A_1^p = 2(\lambda_d(\lambda_s(\beta_d f_d\xi_d+(\mu_2+1)\xi_1)+\xi_1(\mu_2+\mu_s))+\lambda_2(\lambda_d(\beta_d f_d\xi_d+\xi_1(\mu_s+1))+\beta_d f_d\xi_d(\lambda_s+1)) \\ \quad +\beta_d f_d\xi_d\lambda_s) \\ A_2^p = \beta_d(4\xi_1 f_d(\lambda_d+1)\xi_d(\mu_2+\mu_s)+\lambda_s(4(\mu_2+1)\xi_1 f_d\xi_d+\lambda_d+1)+\lambda_2(4\xi_1 f_d\xi_d+4\xi_1 f_d\xi_d\mu_s+\lambda_d \\ \quad +\lambda_s+1))+\lambda_d(\lambda_2+4\mu_2\xi_1^2+\beta_2(\lambda_s+1)+\lambda_s+4\mu_2\xi_1^2\mu_s+4\xi_1^2\mu_s) \\ A_3^p = 2(\beta_d(\beta_2 f_d\lambda_d\xi_d+\beta_2 f_d\xi_d+4\mu_2\xi_1^2 f_d\xi_d+\lambda_s((\beta_2+1)f_d\xi_d+(\mu_2+1)\xi_1)+\lambda_2(f_d\xi_d+\xi_1(\mu_s+1)) \\ \quad +4\xi_1^2 f_d\xi_d\mu_s+4\mu_2\xi_1^2 f_d\xi_d\mu_s+\mu_2\xi_1\lambda_d+\xi_1\lambda_d\mu_s+\mu_2\xi_1+\xi_1\mu_s)+\xi_1\lambda_d(\mu_2+\beta_2(\mu_s+1)+\mu_s)) \\ A_4^p = \beta_2(\beta_d(4\xi_1 f_d\xi_d+4\xi_1 f_d\xi_d\mu_s+\lambda_d+\lambda_s+1)+\lambda_d)+\beta_d(4\xi_1(\mu_s(f_d\xi_d+\xi_1)+\mu_2(f_d\xi_d+\xi_1(\mu_s+1))) \\ \quad +\lambda_2+\lambda_s) \\ A_5^p = 2\beta_d(\beta_2(f_d\xi_d+\xi_1(\mu_s+1))+\xi_1(\mu_2+\mu_s)) \\ A_6^p = \beta_2\beta_d \end{cases} \tag{C2}$$

Appendix D. The numerator coefficient of Eq. (10) is as follows:

$$\begin{cases} C_0^p = \lambda_d((\beta_d+1)\lambda_s+\beta_2(\lambda_s+1)) \\ C_1^p = 2(\beta_2(\lambda_d(\beta_d f_d\xi_d+\xi_1(\mu_s+1))+\beta_d f_d\xi_d(\lambda_s+1))+\beta_d f_d\xi_d\lambda_s+\xi_1(\beta_d+1)\lambda_d\mu_s) \\ C_2^p = \beta_d(4\xi_1 f_d\xi_d\mu_s+\lambda_s)+\beta_2(\beta_d(4\xi_1 f_d\xi_d+4\xi_1 f_d\xi_d\mu_s+\lambda_d+\lambda_s+1)+\lambda_d) \\ C_3^p = 2\beta_d(\beta_2(f_d\xi_d+\xi_1(\mu_s+1))+\xi_1\mu_s) \\ C_4^p = \beta_2\beta_d \end{cases} \tag{D1}$$

Appendix E. Using the Residue Theorem, the evaluation index PI can be calculated by the following formula:

$$PI = \frac{1}{2\pi}\int_{-\infty}^{+\infty}\left|-\frac{B_4(i\alpha)^4+B_3(i\alpha)^3+B_2(i\alpha)^2+B_1(i\alpha)+B_0}{A_6(i\alpha)^6+A_5(i\alpha)^5+A_4(i\alpha)^4+A_3(i\alpha)^3+A_2(i\alpha)^2+A_1(i\alpha)+A_0}\right|^2 d\alpha = \frac{Num}{Den} \tag{E1}$$

where

$$
\begin{aligned}
Num = & -B_5{}^2(-A_6A_3A_1A_0 + A_6A_2A_1{}^2 - A_5{}^2A_0{}^2 + 2A_5A_4A_1A_0 + A_5A_3A_2A_0 - A_5A_2{}^2A_1 - A_4{}^2A_1{}^2 \\
& - A_4A_3{}^2A_0 + A_4A_3A_2A_1) + A_6(B_4{}^2 - 2B_5B_3)(-A_5A_1A_0 + A_4A_1{}^2 + A_3{}^2A_0 - A_3A_2A_1) \\
& + A_6(-B_3{}^2 + 2B_4B_2 - 2B_5B_1)(-A_6A_1{}^2 - A_5A_3A_0 + A_5A_2A_1) + A_6(B_2{}^2 - 2B_3B_1 + 2B_4B_0) \\
& \times (A_6A_3A_1 + A_5{}^2A_0 - A_5A_4A_1) + A_6(-B_1{}^2 + 2B_2B_0)(A_6A_5A_1 - A_6A_3{}^2 - A_5{}^2A_2 + A_5A_4A_3) \\
& + \frac{A_6B_0{}^2}{A_0}(A_6{}^2A_1{}^2 + A_6A_5A_3A_0 - 2A_6A_5A_2A_1 - A_6A_4A_3A_1 + A_6A_3{}^2A_2 - A_5{}^2A_4A_0 \\
& + A_5{}^2A_2{}^2 + A_5A_4{}^2A_1 - A_5A_4A_3A_2)
\end{aligned} \tag{E2}
$$

$$
\begin{aligned}
Den = & 2A_6(A_6{}^2A_1{}^3 + 3A_6A_5A_3A_1A_0 - 2A_6A_5A_2A_1{}^2 - A_6A_4A_3A_1{}^2 - A_6A_3{}^3A_0 + A_6A_3{}^2A_2A_1 + A_5{}^3A_0{}^2 \\
& - 2A_5{}^2A_4A_1A_0 - A_5{}^2A_3A_2A_0 + A_5{}^2A_2{}^2A_1 + A_5A_4{}^2A_1{}^2 + A_5A_4A_3{}^2A_0 - A_5A_4A_3A_2A_1)
\end{aligned} \tag{E3}
$$

Appendix F. In Eq. (12), the specific forms of P_n^s ($n = 1,2,3,4$) and Q_n^s ($n = 1,2,3,4$) are:

$$
\begin{cases}
P_1^s = 4\beta_d^3(\lambda_s + \lambda_2(\lambda_s + 1))^3 \\
P_2^s = 4\beta_d^2(\lambda_s + \lambda_2(\lambda_s + 1))^2 \\
P_3^s = 4\beta_d(\lambda_s + \lambda_2(\lambda_s + 1)) \\
P_4^s = \beta_d(\lambda_s + \lambda_2(\lambda_s + 1))^2
\end{cases} \tag{F1}
$$

$$
\begin{cases}
Q_1^s = (2\beta_2^3\lambda_s(\lambda_s + 1)((\beta_d + 2)\lambda_s + 1) + \beta_2^2\lambda_s(\lambda_2(\beta_d + 1)((\beta_d + 3)\lambda_s + 2) + \lambda_s(\beta_d^2\lambda_s + \beta_d(6\lambda_s + 2) + 6\lambda_s \\
\qquad + 3)) + 2\beta_2(\beta_d + 1)\lambda_s(\lambda_2 + \lambda_s)(\lambda_2(\beta_d + 1) + (\beta_d + 2)\lambda_s) + (\beta_d + 1)^2(\lambda_2 + \lambda_s)^3 + \beta_2^4(\lambda_s + 1)^3) \\
Q_2^s = (\beta_2^2\lambda_s((\beta_d + 6)\lambda_s + 4) + 2\beta_2\lambda_s(\lambda_2(\beta_d + 2) + (\beta_d + 3)\lambda_s) + (\beta_d + 2)(\lambda_2 + \lambda_s)^2 + 2\beta_2^3(\lambda_s + 1)^2) \\
Q_3^s = \lambda_2 + \beta_2^2(\lambda_s + 1) + 2\beta_2\lambda_s + \lambda_s \\
Q_4^s = (\beta_2^2\lambda_s((\beta_d + 3)\lambda_s + 2) + \beta_2\lambda_s(2\lambda_2(\beta_d + 1) + (2\beta_d + 3)\lambda_s) + (\beta_d + 1)(\lambda_2 + \lambda_s)^2 + \beta_2^3(\lambda_s + 1)^2)
\end{cases} \tag{F2}
$$

Appendix G. In Eq. (13), the specific forms of M_n^s ($n = 1,2,3,4$) and N_n^s ($n = 1,2,3,4$) are:

$$
\begin{cases}
M_1^s = 4\beta_d^3\lambda_s^2(\lambda_s + \lambda_2(\lambda_s + 1))^3 \\
M_2^s = 4\beta_d^2\lambda_s^2(\lambda_s + \lambda_2(\lambda_s + 1))^2 \\
M_3^s = 4\beta_d\lambda_s^2(\lambda_s + \lambda_2(\lambda_s + 1)) \\
M_4^s = \beta_d\lambda_s^2(\lambda_s + \lambda_2(\lambda_s + 1))^2
\end{cases} \tag{G1}
$$

$$\begin{cases} N_1^s = 2\beta_2\beta_d^2\lambda_s^5 + \beta_d^2\lambda_s^5 + 2\beta_d\lambda_s^5 + \beta_d^2\lambda_2\lambda_s^4 + 2\beta_d\lambda_2\lambda_s^4 + 6\beta_2^2\beta_d\left(\lambda_s+1\right)\lambda_s^4 + \left(\lambda_2+\lambda_s\right)\lambda_s^4 + 2\beta_2(2\lambda_s+1)\lambda_s^4 \\ \quad + 2\beta_2\beta_d(3\lambda_s+1)\lambda_s^4 + \beta_2^2\beta_d^2(\lambda_s^3+1)\lambda_s^2 + 2\beta_2^3\beta_d(\lambda_s-1)(\lambda_s+1)^3\lambda_s - \beta_2^2\beta_d^2\lambda_2(\lambda_s-2)(\lambda_s+1)^2\lambda_s \\ \quad - 2\beta_2^2\beta_d\lambda_2(\lambda_s+1)^2(2\lambda_s-1)\lambda_s + \beta_2^4(\lambda_s+1)^5 - 2\beta_2^3\beta_d\lambda_2(\lambda_s+1)^4 + \beta_2^2\beta_d^2\lambda_2^2(\lambda_s+1)^3 \\ \quad + 2\beta_2^2\beta_d\lambda_2^2(\lambda_s+1)^3 + 2\beta_2^3(\lambda_s+1)^3(2\lambda_s^2 - \lambda_2(\lambda_s+1)) + \beta_2^2(\lambda_s+1)(3(2\lambda_s+1)\lambda_s^3 \\ \quad - 3\lambda_2(\lambda_s+1)\lambda_s^2 + \lambda_2^2(\lambda_s+1)^2) \\ N_2^s = (\beta_d+2)\lambda_s^4 + 2\beta_2^3(\lambda_s+1)^4 - \beta_2^2(\lambda_s+1)^2(2(\beta_d+2)\lambda_2(\lambda_s+1) - \lambda_s(\beta_d(\lambda_s-2)+6\lambda_s)) \\ \quad + 2\beta_2(((\beta_d+3)\lambda_s+2)\lambda_s^3 - \lambda_2(\lambda_s+1)(\beta_d(\lambda_s-1)+2\lambda_s)\lambda_s + (\beta_d+1)\lambda_2^2(\lambda_s+1)^2) \\ N_3^s = \lambda_s^3 - \lambda_2\lambda_s^2 + \beta_2^2\left(\lambda_s+1\right)^3 + \lambda_2^2\left(\lambda_s+1\right) - 2\beta_2\left(\lambda_s+1\right)\left(\lambda_2\left(\lambda_s+1\right) - \lambda_s^2\right) \\ N_4^s = (\beta_d+1)\lambda_s^4 + \beta_2^3\left(\lambda_s+1\right)^4 - \beta_2^2\left(\lambda_s+1\right)^2(2(\beta_d+1)\lambda_2(\lambda_s+1) - \lambda_s(\beta_d(\lambda_s-2)+3\lambda_s)) \\ \quad + \beta_2((\beta_d^2 + 2\lambda_s^2\beta_d + \lambda_s(3\lambda_s+2))\lambda_s^2 + 2(\beta_d+1)\lambda_2(\beta_d-\lambda_s)(\lambda_s+1)\lambda_s + (\beta_d+1)^2\lambda_2^2(\lambda_s+1)^2) \end{cases} \tag{G2}$$

Appendix H. In Eq. (14), the specific forms of P_1^p, Q_n^p ($n = 1,2,3,4$) are:

$$P_1^p = 4\beta_d(\lambda_s + \lambda_2(\lambda_s+1)) \tag{H1}$$

$$\begin{cases} Q_1^p = (\beta_2+1)\beta_d \\ Q_2^p = -2\beta_2 - \beta_d - 2 \\ Q_3^p = (\lambda_2+1)\beta_d \\ Q_4^p = 2\beta_2(\beta_d+1)\lambda_s + (\beta_d+1)^2(\lambda_2+\lambda_s) + \beta_2^2(\lambda_s+1) \end{cases} \tag{H2}$$

Appendix I. In Eq. (15), the specific forms of M_n^p ($n = 1,2,3,4,5$) and N_n^p ($n = 1,2,3,4,5,6$) are:

$$\begin{cases} M_1^p = \beta_2\lambda_s^2 \\ M_2^p = \lambda_s^2 \\ M_3^p = 4\beta_2^2\lambda_s^2 \\ M_4^p = 4\beta_2\lambda_s^2 \\ M_5^p = 4\beta_d\lambda_s^2(\lambda_s + \lambda_2(\lambda_s+1)) \end{cases} \tag{I1}$$

$$\begin{cases} N_1^p = \beta_d(\lambda_2^2 + \beta_2^2(\lambda_s+1)^2 + \beta_2(\lambda_s^2 - 2\lambda_2(\lambda_s+1))) \\ N_2^p = 2\beta_d(\beta_2(\lambda_s+1) - \lambda_2) \\ N_3^p = \beta_2\beta_d \\ N_4^p = \beta_d(\beta_2^2(\lambda_s+1)(\lambda_s+\lambda_2(\lambda_s+1)) - 2\beta_2\lambda_2(\lambda_s+\lambda_2(\lambda_s+1)) + \lambda_2^2(\lambda_2+\lambda_s)) \\ N_5^p = -2\lambda_2^2(\beta_d+1) + \beta_2(\beta_d+2)(2\lambda_2(\lambda_s+1) - \lambda_s^2) - 2\beta_2^2(\lambda_s+1)^2 \\ N_6^p = -2\beta_2(\beta_d+1)(\lambda_2(\lambda_s+1) - \lambda_s^2)(\lambda_s+1) + (\beta_d+1)^2(\lambda_s^3 - \lambda_2\lambda_s^2 + \lambda_2^2(\lambda_s+1)) \\ \qquad + \beta_2^2(\lambda_s+1)^3 \end{cases} \tag{I2}$$

Appendix J. The specific forms of R_n ($n = 1, 2, \ldots, 10$) are:

$$R_1 = M_1^p M_3^p M_4^p M_5^p N_3^p \tag{J1}$$

$$R_2 = M_1^p M_3^p M_4^p M_5^p N_2^p \tag{J2}$$

$$R_3 = M_2^p M_3^p M_4^p M_5^p N_1^p \tag{J3}$$

$$R_4 = M_1^p M_2^p M_3^p M_4^p N_6^p \tag{J4}$$

$$R_5 = M_1^p M_2^p M_3^p M_5^p N_5^p \tag{J5}$$

$$R_6 = M_1^p M_2^p M_4^p M_5^P N_4^p \tag{J6}$$

$$R_7 = -M_1^p M_3^p M_4^p N_2^p \tag{J7}$$

$$R_8 = 2M_2^p M_3^p M_4^p N_1^p \tag{J8}$$

$$R_9 = M_1^p M_2^p M_3^p N_5^p \tag{J9}$$

$$R_{10} = 2M_1^p M_2^p M_4^p N_4^p \tag{J10}$$

Appendix K. The optimization results Eq. (26) can be obtained by solving Eq. (24), where the specific form of polynomial R_n ($n = 1, 2, \ldots, 10$) are as follows:

$$U_1 = 12(R_4R_7 - R_1R_9) \tag{K1}$$

$$U_2 = 4(R_4R_8 + R_2R_9 + R_1R_{10} - R_5R_7) \tag{K2}$$

$$\begin{aligned} U_3 = {} & 2R_5^3R_7^3 - 9R_4R_5R_6R_7^3 + 3R_4R_5^2R_8R_7^2 - 18R_4^2R_6R_8R_7^2 - 6R_2R_5^2R_9R_7^2 + 9R_3R_4R_5R_9R_7^2 \\ & + 9R_2R_4R_6R_9R_7^2 + 9R_1R_5R_6R_9R_7^2 - 27R_3R_4^2R_{10}R_7^2 - 6R_1R_5^2R_{10}R_7^2 + 9R_2R_4R_5R_{10}R_7^2 \\ & + 9R_1R_4R_6R_{10}R_7^2 - 3R_4^2R_5R_8^2R_7 - 9R_2R_3R_4R_9^2R_7 + 6R_2^2R_5R_9^2R_7 - 9R_1R_3R_5R_9^2R_7 \\ & - 9R_1R_2R_6R_9^2R_7 - 9R_1R_2R_4R_{10}^2R_7 + 6R_1^2R_5R_{10}^2R_7 - 9R_3R_4^2R_8R_9R_7 - 9R_1R_5^2R_8R_9R_7 \\ & + 3R_2R_4R_5R_8R_9R_7 + 45R_1R_4R_6R_8R_9R_7 - 9R_2R_4^2R_8R_{10}R_7 + 3R_1R_4R_5R_8R_{10}R_7 - 9R_2^2R_4R_9R_{10}R_7 \end{aligned}$$

$$+45R_1R_3R_4R_9R_{10}R_7+3R_1R_2R_5R_9R_{10}R_7-9R_1^2R_6R_9R_{10}R_7-2R_4^3R_8^3-2R_2^3R_9^3+9R_1R_2R_3R_9^3$$
$$-2R_1^3R_{10}^3-6R_2^2R_4R_8R_9^2+9R_1R_3R_4R_8R_9^2+9R_1R_2R_5R_8R_9^2-27R_1^2R_6R_8R_9^2-6R_1^2R_4R_8R_{10}^2$$
$$+3R_1^2R_2R_9R_{10}^2-6R_2R_4^2R_8^2R_9+9R_1R_4R_5R_8^2R_9-6R_1R_4^2R_8^2R_{10}+3R_1R_2^2R_9^2R_{10}-18R_1^2R_3R_9^2R_{10}$$
$$-3R_1R_2R_4R_8R_9R_{10}+9R_1^2R_5R_8R_9R_{10} \tag{K3}$$

$$U_4=4(3(R_1R_9-R_4R_7)(-R_6R_7+R_5R_8+R_3R_9+R_2R_{10})-(-R_5R_7+R_4R_8+R_2R_9+R_1R_{10})^2)^3$$
$$+\ (-2R_5^3R_7^3+9R_1R_2R_6R_9^2R_7+9R_1^2R_6R_9R_{10}R_7-3R_5^2(R_4R_7R_8-2R_2R_7R_9$$
$$-R_1(3R_8R_9+2R_7R_{10}))R_7+2R_4^3R_8^3+2R_2^3R_9^3-9R_1R_2R_3R_9^3+2R_1^3R_{10}^3+27R_1^2R_6R_8R_9^2$$
$$-3R_1^2R_2R_9R_{10}^2-3R_1R_2^2R_9^2R_{10}+18R_1^2R_3R_9^2R_{10}-3R_5(R_{10}(3R_8R_9+2R_7R_{10})R_1^2$$
$$+R_9(3R_6R_7^2-3R_3R_9R_7+R_2(3R_8R_9+R_7R_{10}))R_1-R_4^2R_7R_8^2+2R_2^2R_7R_9^2$$
$$+R_4(-3R_6R_7^3+3R_3R_9R_7^2+3R_2R_{10}R_7^2+R_2R_8R_9R_7+R_1R_8R_{10}R_7+3R_1R_8^2R_9))+3R_4^2(6R_6R_8R_7^2$$
$$+3R_3(R_8R_9+3R_7R_{10})R_7+R_8(2R_1R_8R_{10}+R_2(2R_8R_9+3R_7R_{10})))3R_4(R_9(2R_8R_9+3R_7R_{10})R_2^2$$
$$+(-3R_6R_9R_7^2+3R_3R_9^2R_7+R_1R_{10}(R_8R_9+3R_7R_{10}))R_2+R_1(2R_1R_8R_{10}^2-3R_6R_7(5R_8R_9+R_7R_{10})$$
$$-3R_3R_9(R_8R_9+5R_7R_{10}))))^2 \tag{K4}$$

$$U_5=R_5^2R_7^2+3R_1R_6R_9R_7+R_4^2R_8^2+R_2^2R_9^2-3R_1R_3R_9^2+R_1^2R_{10}^2-R_1R_2R_9R_{10}+R_4(-3R_6R_7^2+3R_3R_9R_7$$
$$+3R_2R_{10}R_7+2R_2R_8R_9+2R_1R_8R_{10})+R_5(R_4R_7R_8-2R_2R_7R_9-R_1(3R_8R_9+2R_7R_{10})) \tag{K5}$$

Here, it is necessary to point out the calculation process of the optimum solutions f_{dopt} and ξ_{dopt} under parallel TID coupling in Table 4.

Substituting Eqs. (I1), (I2), (20), (J1)–(J10) and (K1)–(K5) into Eq. (26), the calculated result is:

$$\begin{cases} f_d=1.077742289697411-1.766960131585629\times10^{-15}i \\ \xi_d=0.11978984818672636-2.6187984688434\times10^{-15}i \end{cases} \tag{K6}$$

In the above Equation, i is the imaginary unit, omit the smallest imaginary part and keep three decimal places, and get the optimum solutions in Table 4.

Appendix L. In Eq. (31), the specific forms of P_n ($n=1,2,3,4$) and Q_n ($n=1,2,3,4$) are:

$$\begin{cases} P_1=4(\lambda_s+\lambda_2(\lambda_s+1))^3\beta_t^3 \\ P_2=4(\lambda_s+\lambda_2(\lambda_s+1))^2\beta_t^2 \\ P_3=4(\lambda_s+\lambda_2(\lambda_s+1))\beta_t \\ P_4=(\lambda_s+\lambda_2(\lambda_s+1))^2\beta_t \end{cases} \tag{L1}$$

$$\begin{cases} Q_1 = \beta_2^4 (\lambda_s + 1)^3 + 2\beta_2^3\lambda_s(2\lambda_s^2 + 3\lambda_s + 1)(\beta_t + 1) + \beta_2^2\lambda_s(3\lambda_s(2\lambda_s + 1) + \lambda_2(3\lambda_s + 2))(\beta_t + 1)^2 \\ \quad + 2\beta_2\lambda_s(\lambda_2^2 + 3\lambda_2\lambda_s + 2\lambda_s^2)(\beta_t + 1)^3 + (\lambda_2 + \lambda_s)^3(\beta_t + 1)^4 \\ Q_2 = 2\beta_2^3 (\lambda_s + 1)^2 + \beta_2^2\lambda_s(3\lambda_s + 2)(\beta_t + 2) + 2\beta_2\lambda_s(2\lambda_2 + 3\lambda_s)(\beta_t + 1) - (\lambda_2 + \lambda_s)^2 (\beta_t - 2) \\ \quad \times (\beta_t + 1)^2 \\ Q_3 = \lambda_2 + \beta_2^2(\lambda_s + 1) + 2\beta_2\lambda_s + \lambda_s \\ Q_4 = \beta_2^3(\lambda_s + 1)^2 + \beta_2^2\lambda_s(3\lambda_s + 2)(\beta_t + 1) + \beta_2\lambda_s(2\lambda_2 + 3\lambda_s)(\beta_t + 1)^2 + (\lambda_2 + \lambda_s)^2(\beta_t + 1)^3 \end{cases} \tag{L2}$$

Appendix M. In Eq. (33), the specific forms of M_n (n = 1,2,3,4) and N_n (n = 1,2,3,4) are:

$$\begin{cases} M_1 = 4\lambda_s^2 (\lambda_s + \lambda_2 (\lambda_s + 1))^3 \beta_t^3 \\ M_2 = 4\lambda_s^2 (\lambda_s + \lambda_2 (\lambda_s + 1))^2 \beta_t^2 \\ M_3 = 4\lambda_s^2 (\lambda_s + \lambda_2 (\lambda_s + 1)) \beta_t \\ M_4 = \lambda_s^2 (\lambda_s + \lambda_2 (\lambda_s + 1))^2 \beta_t \end{cases} \tag{M1}$$

$$\begin{cases} N_1 = \beta_2^4 (\lambda_s + 1)^5 - 2\beta_2^3(\lambda_2(\lambda_s + 1) - 2\lambda_s^2) (\lambda_s + 1)^3 (\beta_t + 1) + \beta_2^2(3(2\lambda_s + 1)\lambda_s^3 - 3\lambda_2(\lambda_s + 1)\lambda_s^2 \\ \quad + \lambda_2^2(\lambda_s + 1)^2)(\lambda_s + 1)(\beta_t + 1)^2 + \lambda_s^4(\lambda_2 + \lambda_s)(\beta_t + 1)^4 + 2\beta_2\lambda_s^4(2\lambda_s + 1)(\beta_t + 1)^3 \\ N_2 = -2\beta_2^3 (\lambda_s + 1)^4 + \lambda_s^4(\beta_t - 2) (\beta_t + 1)^2 + \beta_2^2 (\lambda_s + 1)^2 (2\lambda_2(\lambda_s + 1) - 3\lambda_s^2)(\beta_t + 2) - 2\beta_2 \\ \quad \times((3\lambda_s + 2)\lambda_s^3 - 2\lambda_2(\lambda_s + 1)\lambda_s^2 + \lambda_2^2(\lambda_s + 1)^2)(\beta_t + 1) \\ N_3 = \beta_2^2(\lambda_s + 1)^3 - 2\beta_2(\lambda_s + 1)(\lambda_2(\lambda_s + 1) - \lambda_s^2) + \lambda_s^3 - \lambda_2\lambda_s^2 + \lambda_2^2(\lambda_s + 1) \\ N_4 = \beta_2^3 (\lambda_s + 1)^4 + \lambda_s^4 (\beta_t + 1)^3 - \beta_2^2 (\lambda_s + 1)^2 (2\lambda_2(\lambda_s + 1) - 3\lambda_s^2)(\beta_t + 1) + \beta_2((3\lambda_s + 2)\lambda_s^3 \\ \quad - 2\lambda_2(\lambda_s + 1)\lambda_s^2 + \lambda_2^2(\lambda_s + 1)^2)(\beta_t + 1)^2 \end{cases} \tag{M2}$$